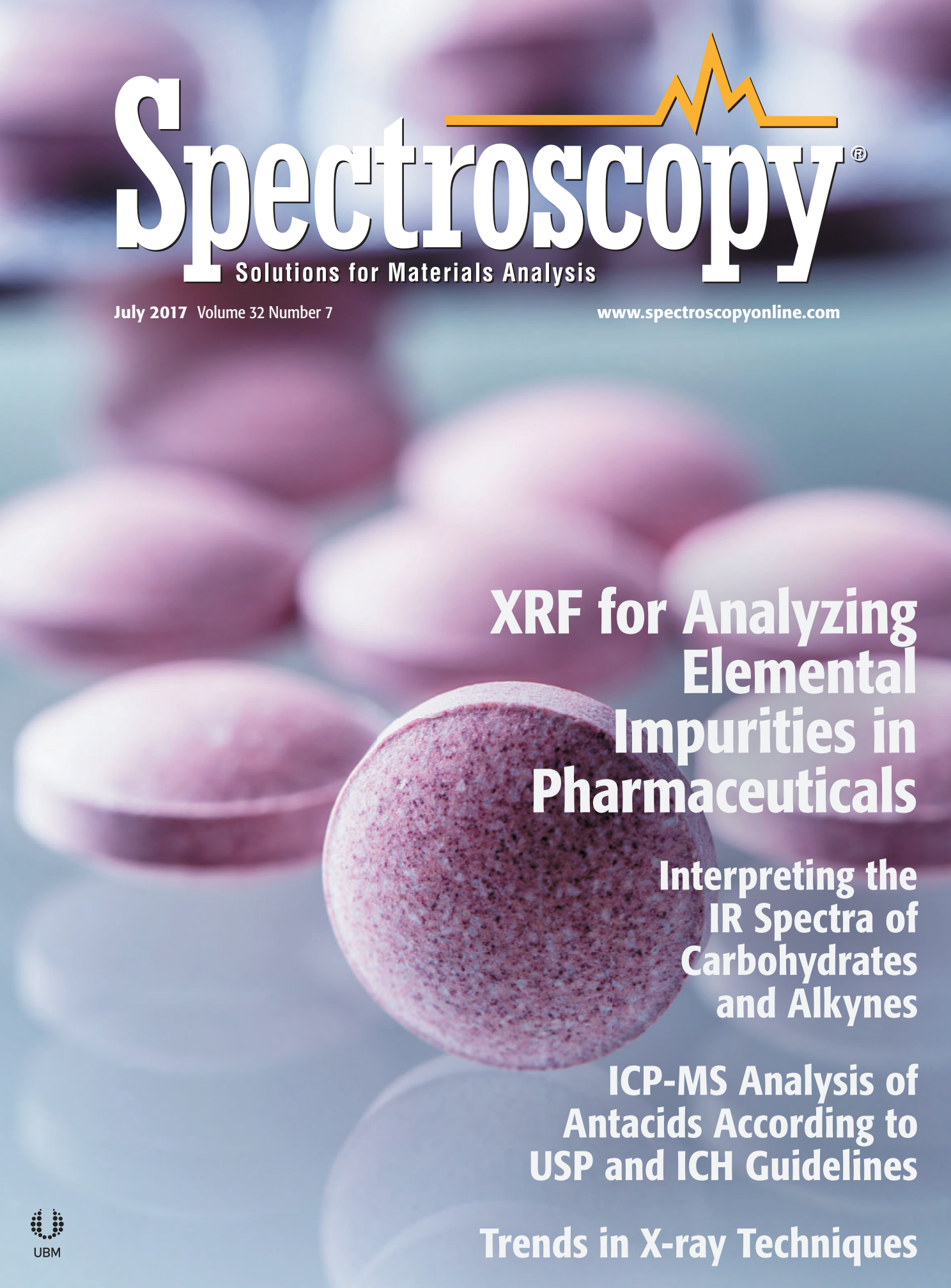

Spectroscopy®

Solutions for Materials Analysis

July 2017 Volume 32 Number 7

www.spectroscopyonline.com

XRF for Analyzing Elemental Impurities in Pharmaceuticals

Interpreting the IR Spectra of Carbohydrates and Alkynes

ICP-MS Analysis of Antacids According to USP and ICH Guidelines

Trends in X-ray Techniques

UBM

GET MORE SPECTRAL DATA IN LESS TIME

The Ocean FX Spectrometer Offers Fast Acquisition Speed, Robust Communications and Spectral Buffering

25 YEARS
OF CUSTOMER PARTNERSHIP

HIGH-SPEED ACQUISITION

Acquire and process more spectral data in less time

Fast acquisition rate for high-intensity irradiance

ROBUST INTERFACE

Operates via Gigabit Ethernet, Wi-Fi and USB

Ideal for remote sensing and handheld monitoring

SPECTRAL BUFFERING

Onboard buffer holds up to 50,000 spectra so you don't miss a single data point

Ensures data integrity in applications like chemical kinetics

See the latest in high-speed miniature spectroscopy at Booth #1525 of the ACS National Meeting & Expo, Aug. 21-24, 2017 in Washington, D.C.

ACS Chemistry for Life®

Ocean Optics

info@oceanoptics.com • www.oceanoptics.com • **US** +1 727-733-2447
EUROPE +31 26-3190500 • **ASIA** +86 21-6295-6600

HORIBA
Scientific

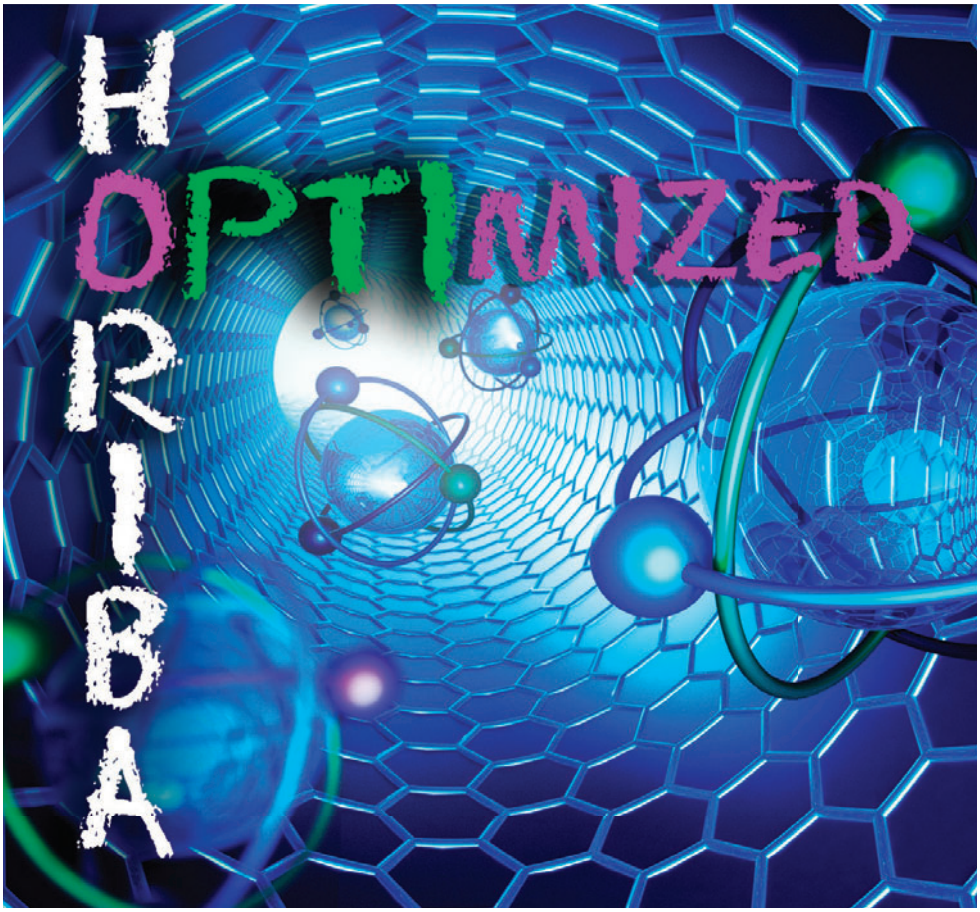

Why compromise when you can o**PTI**mize?

In the two years since PTI joined the HORIBA family, we have been at our drawing boards developing the newest, and most comprehensive modular research steady state fluorometers on the market.

Our new **PTI QuantaMaster 8000** series includes everything you need for unlimited flexibility, unprecedented adaptability, and the highest guaranteed sensitivity on the market with a SNR > 30,000:1 !

Of course, if you want NIR spectra and phosphorescence out to 5,500 nm, 100MHz TCSPC, or a microscopy upgrade, you can have those, too, and much more.

The new PTI QuantaMaster 8000 series can do more than any other spectrofluorometer out there, and will do it better and more accurately. So, don't compromise...
o**PTI**mize with the new PTI QuantaMaster 8000 series.

It's all your lab will ever need.

quantamaster.com
email: ad.sci@horiba.com

JOBIN YVON Technology

MANUSCRIPTS: To discuss possible article topics or obtain manuscript preparation guidelines, contact the editorial director at: (732) 346-3020, e-mail: Laura.Bush@ubm.com. Publishers assume no responsibility for safety of artwork, photographs, or manuscripts. Every caution is taken to ensure accuracy, but publishers cannot accept responsibility for the information supplied herein or for any opinion expressed.
SUBSCRIPTIONS: For subscription information: *Spectroscopy,* P.O. Box 6196, Duluth, MN 55806-6196; (888) 527-7008, 7:00 a.m. to 6:00 p.m. CST. Outside the U.S., +1-218-740-6477. Delivery of *Spectroscopy* outside the U.S. is 3–14 days after printing. Single-copy price: U.S., $10.00 + $7.00 postage and handling ($17.00 total); Canada and Mexico, $12.00 + $7.00 postage and handling ($19.00 total); Other international, $15.00 + $7.00 postage and handling ($22.00 total).
CHANGE OF ADDRESS: Send change of address to *Spectroscopy,* P.O. Box 6196, Duluth, MN 55806-6196; provide old mailing label as well as new address; include ZIP or postal code. Allow 4–6 weeks for change. Alternately, go to the following URL for address changes or subscription renewal: http://ubmsubs.ubm.com/?pubid=SPEC
RETURN ALL UNDELIVERABLE CANADIAN ADDRESSES TO: IMEX Global Solutions, P.O. Box 25542, London, ON N6C 6B2, CANADA. PUBLICATIONS MAIL AGREEMENT No.40612608.
REPRINT SERVICES: Reprints of all articles in this issue and past issues are available (500 minimum). Call 877-652-5295 ext. 121 or e-mail bkolb@wrightsmedia.com. Outside US, UK, direct dial: 281-419-5725. Ext. 121
C.A.S.T. DATA AND LIST INFORMATION: Contact Melissa Stillwell, (218) 740-6831; e-mail: Melissa.Stillwell@ubm.com
INTERNATIONAL LICENSING: Maureen Cannon, (440) 891-2742, fax: (440) 891-2650; e-mail: Maureen.Cannon@ubm.com

UBM Americas (www.ubmamericas.com) is a leading worldwide media company providing integrated marketing solutions for the Fashion, Life Sciences and Powersports industries. UBM Americas serves business professionals and consumers in these industries with its portfolio of 91 events, 67 publications and directories, 150 electronic publications and Web sites, as well as educational and direct marketing products and services. Market leading brands and a commitment to delivering innovative, quality products and services enables UBM Americas to "Connect Our Customers With Theirs. UBM Americas has approximately 1000 employees and currently operates from multiple offices in North America and Europe.

485F US Highway One South, Suite 210
Iselin, NJ 08830
(732) 596-0276
Fax: (732) 647-1235

Michael J. Tessalone
Vice President/Group Publisher
Michael.Tessalone@ubm.com

Stephanie Shaffer
Publisher
Stephanie.Shaffer@ubm.com

Edward Fantuzzi
Associate Publisher
Edward.Fantuzzi@ubm.com

Michael Kushner
Senior Director, Digital Media
Michael.Kushner@ubm.com

Laura Bush
Editorial Director
Laura.Bush@ubm.com

Megan L'Heureux
Managing Editor
Meg.L'Heureux@ubm.com

Stephen A. Brown
Group Technical Editor
Stephen.Brown@ubm.com

Cindy Delonas
Associate Editor
Cindy.Delonas@ubm.com

Kristen Moore
Webcast Operations Manager
Kristen.Moore@ubm.com

Vania Oliveira
Project Manager
Vania.Oliveira@ubm.com

Sabina Advani
Digital Production Manager
Sabina.Advani@ubm.com

Kaylynn Chiarello-Ebner
Managing Editor, Special Projects
Kaylynn.Chiarello.Ebner@ubm.com

Dan Ward
Art Director
dward@hcl.com

Anne Lavigne
Marketing Manager
Anne.Lavigne@ubm.com

Melissa Stillwell
C.A.S.T. Data and List Information
Melissa.Stillwell@ubm.com

Wright's Media
Reprints
bkolb@wrightsmedia.com

Maureen Cannon
Permissions
Maureen.Cannon@ubm.com

Jesse Singer
Production Manager
jsinger@hcl.com

Wendy Bong
Audience Development Manager
Wendy.Bong@ubm.com

Ross Burns
Audience Development Assistant Manager
Ross.Burns@ubm.com

Tips for pressing an XRF pellet

A SPECTROSCOPY GUIDE FROM SPECAC

- **Choose the ideal pellet die size**
  common diameters for round XRF pellets are 32 mm or 40 mm
- **Are you milling your sample to a powder?**
  pressed powders must be very fine and with consistent particle size
- **Standard or ring pellet die?**
  automatic loading systems often require ring dies to protect samples
- **Do you have a high-quality pellet die?**
  all XRF dies need a polished, smooth stainless steel pressing face
- **Ensure the correct load for XRF pellet pressing**
  different samples require different loads, anywhere from 2 to 40 tons
- **Manual or automatic hydraulic press?**
  manual = affordable, automatic = higher loads and repeatability

AUTOTOUCH PRESS

Powerful, reliable, robust and only needs minimum maintenance

Li Chen of SCP Science

www.specac.com sales@specac.com UK: +44 (0)1689 892902 USA: +1 866 726 1126

Specac

Spectroscopy

July 2017
Volume 32 Number 7

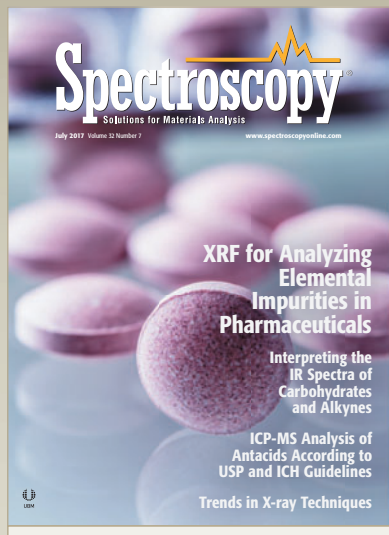

Cover image courtesy of Marian Weyo / shutterstock.com.

DEPARTMENTS

ON THE WEB

QUIZ: INTERPRETING SPECTRA

Take the latest quiz!

Are your spectral interpretation skills up to par? Find out by taking the latest quiz from our "IR Spectral Interpretation Workshop" column.

See the quiz on page 22 of this issue or at:

http://www.spectroscopyonline.com/ir-spectral-interpretation-workshop-0

WEB SEMINARS

How to Achieve Valid Results First Time, Every Time with ICP Techniques
Niel Williams, PhD, and Bill Spence, Teledyne CETAC Technologies

spectroscopyonline.com/SpecWebSeminars

Like *Spectroscopy* on Facebook:
www.facebook.com/SpectroscopyMagazine

Follow *Spectroscopy* on Twitter:
https://twitter.com/spectroscopyMag

Join the *Spectroscopy* Group on LinkedIn
http://linkd.in/SpecGroup

CONTENTS

VOLUME 32 NUMBER 7
JULY 2017

COLUMNS

SPECIAL FEATURE

PEER-REVIEWED ARTICLES

Spectroscopy (ISSN 0887-6703 [print], ISSN 1939-1900 [digital]) is published monthly by UBM LLC 131 West First Street, Duluth, MN 55802-2065. Spectroscopy is distributed free of charge to users and specifiers of spectroscopic equipment in the United States. *Spectroscopy* is available on a paid subscription basis to nonqualified readers at the rate of: U.S. and possessions: 1 year (12 issues), $74.95; 2 years (24 issues), $134.50. Canada/Mexico: 1 year, $95; 2 years, $150. International: 1 year (12 issues), $140; 2 years (24 issues), $250. Periodicals postage paid at Duluth, MN 55806 and at additional mailing offices. POSTMASTER: Send address changes to Spectroscopy, P.O. Box 6196, Duluth, MN 55806-6196. PUBLICATIONS MAIL AGREEMENT NO. 40612608, Return Undeliverable Canadian Addresses to: IMEX Global Solutions, P. O. Box 25542, London, ON N6C 6B2, CANADA. Canadian GST number: R-124213133RT001. Printed in the U.S.A.

SHIMADZU
Excellence in Science

Accelerating Reliable Performance

ICPMS-2030

Inductively Coupled Plasma Mass Spectrometer

Powered by its vast LC-MS/MS and GC-MS/MS experience, Shimadzu has released the **ICPMS-2030**, offering an exceptional combination of ease of use, high sensitivity, and low running costs. Simplify your ICP-MS analysis, and obtain reliable trace-level results with confidence. Choose the ICPMS-2030.

Learn more about Shimadzu's ICPMS-2030.
Call (800) 477-1227 or visit us online at
www.ssi.shimadzu.com/ICPMS

Order consumables and accessories on-line at http://store.shimadzu.com
Shimadzu Scientific Instruments Inc., 7102 Riverwood Dr., Columbia, MD 21046, USA

Key benefits include:

- **Fast, easy method development and acquisition of reliable results** – Analysis assistant functions speed method development and automatically detect and correct isobaric interferences.
- **High sensitivity with no polyatomic interferences** – Newly developed helium collision cell eliminates polyatomic interferences while maintaining high sensitivity.
- **Lowest operation costs of any ICP-MS on the market** – Proprietary mini-torch consumes 2/3 the argon as conventional ICP-MS analyzers; Eco-mode and the ability to use lower purity argon reduce operating costs further.

Elemental Analysis • Environmental • Food & Agriculture • Pharmaceutical

Editorial Advisory Board

Spectroscopy's Editorial Advisory Board is a group of distinguished individuals assembled to help the publication fulfill its editorial mission to promote the effective use of spectroscopic technology as a practical research and measurement tool. With recognized expertise in a wide range of technique and application areas, board members perform a range of functions, such as reviewing manuscripts, suggesting authors and topics for coverage, and providing the editor with general direction and feedback. We are indebted to these scientists for their contributions to the publication and to the spectroscopy community as a whole.

INTERNATIONAL CENTRE FOR DIFFRACTION DATA

Diffraction Data You Can Trust

ICDD databases are the only crystallographic databases in the world with quality marks and quality review processes that are ISO certified.

PDF-4+
Identify + Quantitate

Identify and Quantitate
398,726 Entries
295,309 Atomic coordinates

Digitized patterns

Combines powder and single crystal data

Molecular graphics

Analyze neutron, electron, synchrotron data

Standardized Data

More Coverage

All Data Sets Evaluated For Quality

Reviewed, Edited and Corrected Prior To Publication

Targeted For Material Identification and Characterization

www.icdd.com/products/pdf4.htm

ICDD® International Centre for Diffraction Data

ISO 9001:2008 QUALITY ASSURED COMPANY CERT.NR. 11409.1

www.icdd.com | marketing@icdd.com

News Spectrum

Tunable Diode Laser Spectroscopy Used to Assess Food Quality

A group of researchers from the Center of Optical and Electromagnetic Research at South China Normal University (Guangzhu, China) and the Lund Laser Center at Lund University (Lund, Sweden) used a tunable diode laser spectroscopy technique to detect the oxygen content in packaging for foods such as milk and bread (1). The team used the gas in scattering media absorption spectroscopy (GASMAS) technique and demonstrated its accuracy, stability, and repeatability for the in-line monitoring of food packaging in an industrial setting.

In their paper, the researchers noted that, increasingly, techniques such as modified atmosphere packaging are used with the intention of increasing the shelf life of the product. In that technique, gas mixtures containing gases such as nitrogen and carbon dioxide replace the normal atmospheric air in the package. The paper indicated that the widespread use of "best before" dates on the packaging increases food safety, but that the durability of food and suitability for consumption also strongly depends on ambient storage conditions and the adequacy of the sealing in the packaging machine.

In the search for a real-time, nonintrusive, and cost-effective technique for monitoring the packaging process, different detection geometries were adopted to collect scattering light that had passed through the gas volume in the packages, and to avoid the disturbance of ambient air. The researchers were able to study the bread-baking process by measuring the water vapor signals in fermenting dough.

The results showed that the GASMAS technique has potential for nonintrusive assessment of food quality and in the bread-baking process. It can reproducibly assess the oxygen contents in bread and milk packaging. The study determined that the technique is suitable for providing status information about packaged food in real time.

Reference

(1) T. Li, H. Lin, H. Zhang, K. Svanberg, and S. Svanberg, *Appl. Spectrosc.* **71**(5), 929–938 (2017).

Gordon F. Kirkbright Bursary Award, 2018

Applications are invited for the 2018 Gordon F. Kirkbright Bursary Award. This prestigious award is given annually to enable a promising student or tenured young scientist of any nation to attend a recognized scientific meeting or visit a place of learning.

The fund for this endowment was established in 1985 as a memorial to Professor Gordon Kirkbright in recognition of his contributions to analytical spectroscopy and to science in general. Although the fund is administered by the Association of British Spectroscopists (ABS) Trust, the award is not restricted to spectroscopists.

To download an application form or for further information, visit http://www.abstrust.org or contact abstrustuk@gmail.com.

The closing date for entries is December 31, 2018.

Eurofins to Establish New Facility in Scotland

Eurofins Scientific (Luxembourg), an international group of laboratories, has plans to establish a new pharmaceutical chemistry and microbiology facility in Livingston, Scotland, as part of a £4 million investment.

The 5800-square meter facility at Brucefield Industry Park will house Eurofin's biopharmaceutical testing business in the UK, currently based in Edinburgh. The first phase of the project will include the development of 1400 square meters of laboratory space.

As part of the investment, Eurofins BioPharma Product Testing UK will be purchasing a new inductively coupled plasma–mass spectrometry (ICP-MS) instrument, allowing the company to meet growing demand for this service as a result of new International Conference Harmonization (ICH) guidelines and pharmacopeial chapters on testing drugs for elemental impurities. Eurofins will also invest in more high performance liquid chromatography (HPLC) equipment, increasing that capacity by 40%. ■

IR QUIZ TIME

Using what you have learned from this and other columns, do you best to assign the peaks in the spectrum shown in the figure below of the IR spectrum of a liquid (sampling technique: thin film). Determine the functional groups present, and determine the chemical structure of the molecule that gave rise to this spectrum.

To see the answer, please turn to page 22.

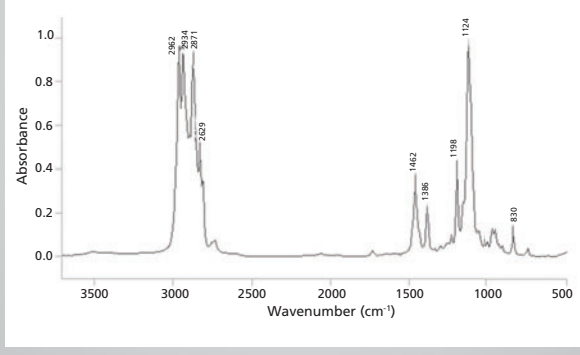

www.spectroscopyonline.com/ir-spectral-interpretation-workshop-quiz-11

Preparing for USP 232/233 compliance?

- Improved workflow
- Exceptional digestion quality
- No batching required
- Lower operating costs

All microwave digestion systems are not created equal.

When it comes to choosing a sample prep instrument for the upcoming USP 232/233 compliance, the Milestone UltraWAVE is in a league of its own.

Patented UltraWAVE Single Reaction Chamber (SRC) technology transcends traditional closed and open vessel systems, offering significantly greater digestion capabilities for even the most difficult sample types. The UltraWAVE delivers superior digestion quality, yielding exceptional ICP-OES or ICP-MS analyses.

High-performance stainless steel construction allows for higher pressures and temperatures over conventional systems. Simplified construction and disposable vials eliminate the need to assemble, disassemble or clean between processing. Just as important, dissimilar samples can be processed simultaneously, saving both time and money.

Learn more about the UltraWAVE and access our USP resources at:
milestonesci.com/pharmaceutical


Ethos UP


UltraWAVE


UltraCLAVE

MILESTONE

Atomic Perspectives

Using XRF as an Alternative Technique to Plasma Spectrochemistry for the New *USP* and *ICH* Directives on Elemental Impurities in Pharmaceutical Materials

New guidelines governing the analysis of elemental impurities in pharmaceuticals are being implemented in the manufacturing of pharmaceutical products. X-ray fluorescence (XRF) spectrometry is a nondestructive analysis technique offering high sensitivity, precision, and accuracy without requiring chemical pretreatment. This installment of "Atomic Perspectives" evaluates the ability of XRF spectrometry to perform elemental impurity analysis of 12 elements in various pharmaceutical materials, such as cellulose, talc, and a mixture of cellulose, talc, and TiO_2, by the calibration curve method using water solution standard samples, and verifying the qualification of *United States Pharmacopeia* (*USP*) *Chapter* <735>.

Daniel Davis and Hiroaki Furukawa

New guidelines governing the analysis of elemental impurities in pharmaceuticals are being implemented. Toxic heavy metals and residual metal catalysts may exist in the raw materials of active pharmaceutical ingredients (APIs) or be added during the manufacturing process, which may be a risk to human health.

In December 2014, *The International Council for Harmonization of Technical Requirements for Pharmaceuticals for Human Use* (*ICH*) issued *Q3D Step 4 Guidelines* (1), which limits 24 elements, including Cd, Pb, As, Hg, V, Co, Ni, Ir, Pt, Rh, Ru, and Pd, in drug products and pharmaceutical ingredients. This guideline has now reached the implementation stage. In May 2015, the *United States Pharmacopeia* (*USP*) established X-ray fluorescence (XRF) methodology as *General Chapter* <735>, "X-ray Fluorescence Spectrometry." XRF spectrometry is a nondestructive analysis technique offering high sensitivity, precision, and accuracy,

typically without requiring lengthy chemical pretreatment (2).

This study assesses the capability of XRF to carry out the determination of these 12 elemental impurities in various pharmaceutical materials, including cellulose, talc, and a mixture of cellulose, talc, and TiO_2, using aqueous-based calibration standards, and verifying the use of *USP Chapter* <735> as a screening tool for this analysis.

Permitted Daily Exposures and Concentration Limits

The *ICH Q3D Step 4 Guidelines* together with *USP Chapter* <232> "Elemental Impurities: Limits" (3), defines permitted daily exposure (PDE) values for oral, parenteral, and inhalational drug products. There are 24 elements included in the risk assessment and they are classified into four groups: Class 1 (Cd, Pb, As, and Hg), Class 2A (V, Co, and Ni), Class 2B (Tl, Au, Pd, Ir, Os, Rh, Ru, Se, Ag, and Pt), and Class 3 (Li, Sb, Ba, Mo, Cu, Sn, and Cr). Class 1 and 2A are very important elements and must be analyzed regardless of whether they are added intentionally or as result of the production process. Class 2B elements are not required to be checked for the risk assessment if these elements are not intentionally added; however, catalyst elements such as Ir, Pt, Rh, Ru, and Pd are commonly used in the process of producing APIs. It is necessary to convert the maximum daily intake to concentration limits because the PDE units are defined in micrograms per day. *ICH Q3D Step 4* gives guidance in converting between PDEs and concentration limits as described below:

1. Option 1 is for common permitted concentration limits of elements across drug product components for drug products with daily intakes of no more than 10 g.
2. Option 2a is for common permitted concentration limits across drug product components for a drug product with a specified daily intake.
3. Option 2b is for permitted concentration limits of elements in individual components of a product with a specified daily intake.
4. Option 3 is for permitted concentration limits from finished product analysis. The most important thing is to change the concentration limits depending on the conversion method. Table I shows the oral concentration limits from PDE by options 1 and 2a for the assessment elements. The maximum daily intake assumes 1.0 g for option 2a.

Table I shows oral drug PDE limits of Class 1, 2A, and 2B elements, together with the converted concentration limits based on 10 g and 1 g per day, daily dosages.

X-ray Fluorescence Spectrometry

The XRF technique, generally speaking, does not require chemical pretreatment, and since it is a nondestructive analysis it can identify and determine the concentrations of elements in solid, powdered, and liquid samples. XRF is capable of measuring a wide elemental range, at levels from below parts per million up to percent concentrations.

There are two types of XRF spectroscopic techniques: wavelength dispersive (WDXRF) and energy dispersive (EDXRF). EDXRF systems comprise an X-ray tube and a semiconductor detector and can simultaneously capture many types of fluorescence X-rays generated from the sample using a multichannel analyzer. EDXRF uses a lower power X-ray source, and will not significantly damage the sample. EDXRF systems are very convenient for users. In addition, EDXRF systems are smaller than WDXRF systems, they do not require any external utilities, such as chillers or gases, they typically use a 100-V power supply, and have no moving parts when measuring.

Quantitation is conducted using external calibration standards containing varying concentrations of elements. XRF calibrations have the advantage of being stable for long periods of time before requiring recalibration, in contrast to other elemental analysis techniques, such as inductively coupled plasma–optical emission spectrometry (ICP-OES) and ICP-mass spectrometry (MS) or atomic absorption spectroscopy (AAS). As the bulk of pharmaceutical materials are organic in nature, the EDXRF technique has the best potential for the nondestructive measurement of the aforementioned 12 elements in drug materials without the need for sample dissolution or chemical pretreatment.

Proposed Elemental Impurities Control Method for Drug Materials

USP Chapter <233> (4) specifies either the use of ICP-OES or ICP-MS for the determination of elemental impurities in pharmaceutical materials, or any other technique as long as it can meet the validation protocols. ICP techniques are typically more sensitive than XRF; however, they require chemical digestion techniques to dissolve the samples before measurements can be carried out. This process is very complicated and labor intensive and can be prone to human error and contamination of the sample. To reduce these time-consuming sample preparation procedures for ICP-OES and ICP-MS, the EDXRF technique can be used as a preliminary screening tool to determine if additional chemical analyses are required.

Furthermore, the XRF method may achieve similar performance for low-level chemical analysis if the measurement time is extended, because the detection limit improves with increasing sampling time. This makes EDXRF a very useful screening method to reduce analysis time and lower cost by minimizing the number of samples requiring precise analysis using ICP-OES or ICP-MS (5).

Sample Preparation

Solid, liquid, and powder samples can be analyzed by XRF with minimal sample preparation. The only preparation requirement is reducing the sample to a size that fits in the

Table I: Permitted daily exposures for oral elemental impurities and limits by options

Element	Class	Oral PDE µg/day	Concentration Limit (10 g/day) (µg/g)	Concentration Limit (1 g/day) (µg/g)
Cadmium (Cd)	1	5	0.5	5.0
Lead (Pb)	1	5	0.5	5.0
Arsenic (As)	1	15	1.5	15
Mercury (Hg)	1	30	3.0	30
Vanadium (V)	2A	100	10	100
Cobalt (Co)	2A	50	5.0	50
Nickel (Ni)	2A	200	20	200
Iridium (Ir)	2B	100	10	100
Platinum (Pt)	2B	100	10	100
Rhodium (Rh)	2B	100	10	100
Ruthenium (Ru)	2B	100	10	100
Palladium (Pd)	2B	100	10	100

Table II: Range of calibration standards used for this study

Sample	Standard Sample for Class 1 and 2A Concentration (µg/g)							Sample	Standard Sample for Class 2B Concentration (µg/g)				
	Cd	Pb	As	Hg	V	Co	Ni		Ir	Pt	Ru	Rh	Pd
1-1	0	0	0	0	0	0	0	2-1	0	0	0	0	0
1-2	0.5	0.5	1.5	3	10	5	20	2-4	10	10	10	10	10
1-3	1	1	3	6	20	10	40	2-5	20	20	20	20	20
1-4	2.5	2.5	7.5	15	50	25	100	2-6	50	50	50	50	50
1-5	5	5	15	30	100	50	200	2-7	100	100	100	100	100

Table III: Range of validation–verification samples used for this study

Sample	Sample for Class 1 and 2A Concentration (µg/g)							Sample	Sample for Class 2B Concentration (µg/g)				
	Cd	Pb	As	Hg	V	Co	Ni		Ir	Pt	Ru	Rh	Pd
Low 1	1.3	1.3	4	9	27	13	45	Low 2	27	27	27	27	27
Middle 1	3	3	9	20	60	30	100	Middle 1	60	60	60	60	60
High 1	5.5	5.5	17	33	110	55	110	High 2	110	110	110	110	110

sample cell or chamber. Basically, the larger the sample volume, the smaller the sampling errors.

Almost all solid samples can be analyzed directly by simply placing them in the sample chamber, while liquid samples are poured in a sample cell, with a supporting film at the bottom. Typical films are made from polypropylene of a few micrometers thickness. The majority of drug materials are in organic matrices and have relatively low X-ray absorption, allowing measurement of the element impurities. Powder samples are placed directly into the sample cell using the tapping method to remove voids in the sample. Coarse powders must be ground to a fine particle size, and nonhomogenous samples should be ground by means of mortar and pestle or a grinding device, such as a mill.

Correction Method

XRF calibration is performed for each element by determining the relationship between measured intensities and concentration using a number of standard samples. In general, the measured intensity is corrected by some spectral deconvolution method because the fluorescence X-ray intensity is affected by sample matrices, sample volume, and sometimes interference from other peaks. These effects are known and well understood, and as a result, several methods have been developed to compensate for them, including the internal and overlap correction methods.

Performance Qualification of *USP Chapter* <735>

USP Chapter <735> was implemented in May 2015. The validation protocol

includes operational qualification (OQ) and performance qualification (PQ) to verify that the system operates within target tolerances using appropriate samples with known spectral properties. OQ checks key operating parameters, such as peak position, detector resolution, and count rate, using specific calibration samples. The purpose of PQ is to determine that the instrument is capable of meeting the user's requirements for all critical-to-quality measurements. These validation and verification protocols include linearity, accuracy and specificity, repeatability, intermediate precision, range, quantification limit, and robustness as described below.

Linearity

Analysts should demonstrate a linear relationship between the analyte concentration and corrected XRF response by preparing no fewer than five standards at concentrations that encompass the anticipated concentration of the test sample. The standard curve then should be evaluated using appropriate statistical methods such as least squares regression. The correlation coefficient (R), y-intercept, and slope of the regression line must be determined. Acceptance criteria: R is not less than 0.99.

Accuracy and Specificity

Analysts can determine accuracy by conducting recovery studies using the appropriate matrix spiked with known concentrations of elements. It also is an acceptable practice to compare assay results obtained using the XRF method under validation to those from an established analytical method. Acceptance criteria: 70–150% recovery.

Repeatability

Analysts should measure the concentrations of three replicates of three separate samples. Acceptance criteria: The relative standard deviation is not more than 20.0%.

Intermediate Precision

Analysts should establish the effect

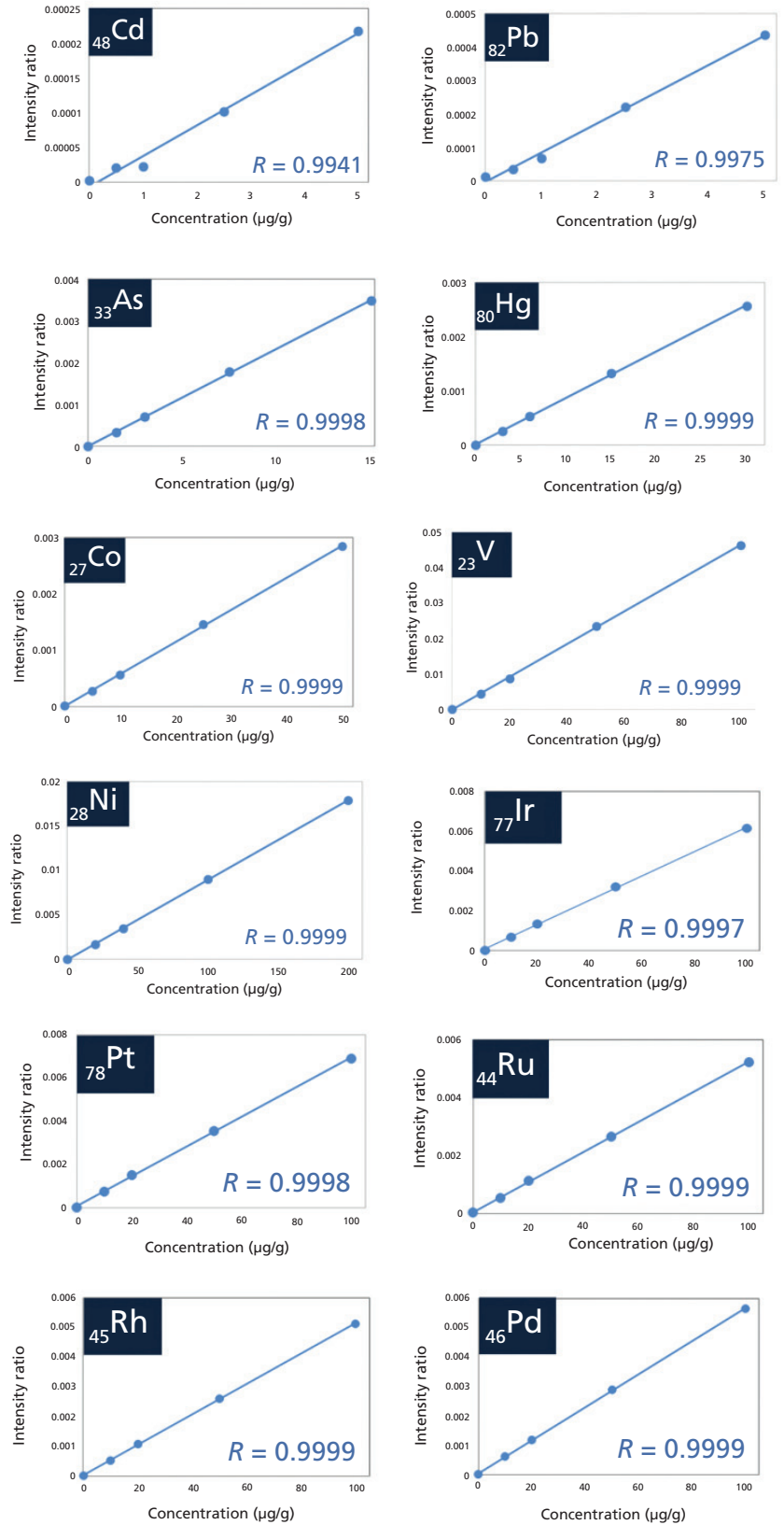

Figure 1: The calibration curves for Cd, Pb, As, Hg, V, Co, Ni, Ir, Pt, Ru, Rh, and Pd.

of random events on the method's analytical precision. Typical variables include performing the analysis on different days, using different instrumentation, or having two or more analysts perform the method. As a minimum, any combination of at least two of these factors totaling six experiments will provide an estimation of intermediate precision. Acceptance criteria: The relative standard deviation (RSD) is not more than 25.0%.

Range

Range is the interval between the upper and lower concentration of an analyte in the sample, which has been demonstrated by meeting the accuracy requirement. 100%-centered acceptance criteria: The range is 80–120%. Noncentered acceptance criteria: 10% below the lower limit of specification to 10% above the upper limit of the specification.

Quantitation Limit

The limit of quantitation (LOQ) can be estimated by calculating the standard deviation of no less than six replicate measurements of a blank and multiplying by 10. Acceptance criteria: The analytical procedure should be capable of determining the analyte precisely and accurately at a level equivalent to 50% of the specification.

Robustness

The reliability of an analytical measurement should be demonstrated by deliberate changes to experimental parameters. Acceptance criteria: The measurement of a standard or sample response following a change in experimental parameters should differ from the same standard measured using established parameters by no more than ±20%.

Experimental

EDXRF spectroscopy measurements were carried out using an EDX-7000 benchtop spectrometer (Shimadzu Scientific Instruments). The spectrometer is equipped with an air-cooled X-ray tube (1000 µA, 50 kV, 50 W) and an electronically cooled silicon-drift detector. The calibration samples and unknown samples were measured using a counting time of 1800 s and an X-ray beam diameter of 10 mm.

The calibration samples were prepared by combining two aqueous stock solutions of Cd, Pb, As, Hg, V, Co, and Ni for Classes 1 and 2A, and Ir, Pt, Ru, Rh, and Pd for Class 2B. These standard solutions were prepared at more than five different concentrations including a blank by dilution with reagent water. The validation and verification samples were prepared from cellulose, talc, and a mixture of cellulose, talc, and titanium oxide powders spiked at three different concentrations with the aforementioned elements using standard solutions for AAS. The standard solutions were added to the above three types of blank powder samples and mixed in an agate mortar to prevent adhesion to the walls.

Next, 8.0 mL of each calibration standard solution together with 2.0-g powder samples were placed directly into a sample cell (32 mm diameter) with a 5-µm polypropylene support film. The powder samples were prepared using a tapping method to settle them in the cell in an effort to reduce voids in the sample packing. Then 1.0-g and 0.5-g powder samples were also placed directly into a sample cell using the tapping method with a 5-µm polypropylene support film for robustness testing. All concentrations of calibration samples were used to generate a calibration curve for each of the above elements. The range of calibration standards together with the validation and verification samples for each element are shown in Tables II and III.

Continuous scattered X-rays at each specific energy range for the above elements were used as an internal standard to correct for sample matrix and volume effects. The quantitation of the impurity elements was calculated by the ratio of fluorescent X-rays for each element with continuous scattered X-rays.

Analytical Results

Linearity

The correlation coefficient of all target elements for the calibration curve meets the acceptance criteria defined in the performance criteria section of *USP Chapter* <735> by using a minimum of five points and achieving a least squares correlation of at least 0.99. Overlap correction was used for As because the energies of AsKα (10.53 keV) and PbLα (10.55 keV) are very close together. The calibration curves for Cd, Pb, As, Hg, V, Co, Ni, Ir, Pt, Ru, Rh, and Pd are shown in Figure 1.

Please see the supplemental online information for Tables sI–sIX described below at: www.spectroscopyonline.com/supplementary-information-Atomic-Perspectives-July-2017.

Tables sI and sII show the accuracy and specificity and range results for Class 1, 2A, and 2B elemental impurities. For the range, the concentration of 100%-centered range (80–120%) defined the concentration limit at a maximum daily intake of 1.0 g from *Chapter* <232> oral drug PDE values; thus, the "High" sample is within the 100%-centered range. For this test, acceptance criteria for accuracy should be 70–150%.

The "Middle" samples are in the noncentered concentration range, and accuracy was interpreted such that it should be within the 63.0–165% range. However, the mixture sample could not validate or verify the V because of overlapping with TiKβ derived from the titanium oxide in the mixture sample.

For the talc sample, the elements at the low-energy region less than 10 eV, such as Hg, Ni, and V, have a low recovery rate because they are influenced by the matrix effect of other major components such as Si and Mg. However, the accuracy, specificity, and range of all target elements and matrices meet the acceptance criteria.

Repeatability

Tables sIII and sIV show the repeat-

ability results. In this test, only the "Middle" samples were checked. The relative standard deviation was calculated from a total of nine data points for each material by measuring three replicates of three separate samples. All target elements and matrices meet the acceptance criteria of <20% RSD.

Intermediate Precision

Tables sV and sVI show the intermediate precision results. In this test, only the "Middle" samples were evaluated. The variable test evaluated two different days, three separate samples, two different EDXRF instruments and two different analysts. It is also valid to apply different combinations of the above events. For example, three analysts can be used if it is difficult to utilize more than two instruments. The relative standard deviation was calculated from a total of 12 data points for each event. All target elements meet the acceptance criteria of <25% RSD.

Quantitation Limits

The quantitation limit was calculated as the standard deviation of the intensity for 10 measurements of a blank cellulose sample. The quantitation limits for all target elements are shown in Table sVII for measurement times of 1800 s, with oral PDE values and control limits in the top four rows. In this investigation the control limit is defined as the PDE limit from *ICH Q3D Step 4 Guidelines*. The concentration limits shown are from conversion method option 2a, based on a dosage of 1 g per day. The two types of control values are based on *USP Chapter* <735> (50% of PDE) and the *ICH Q3D Step 4 Guideline* (30% of PDE). From these data, it can be concluded that the quantitation limit of the EDXRF technique can meet both control limits at 1.0 g maximum daily intake and can successfully perform screening measurements for elemental impurity control at these levels.

Robustness

USP Chapter <735> states that the reliability of an analytical measurement should be demonstrated by evaluating deliberate changes to experimental parameters. In this study, the experimental parameter was defined as sample volume. Tables sVIII and sIX exemplify the robustness results for three different sample volumes, showing the quantitation of 1.0 g and 0.5 g compared to 2.0 g. As demonstrated, all target elements meet the acceptance criteria of ±20%.

Conclusion

This study has shown that EDXRF meets *USP Chapter* <735> acceptance criteria for linearity, accuracy, specificity, range, repeatability, intermediate precision, quantitation limit, and robustness validation protocols. If 1 g per day is the maximum daily intake of a drug product, the technique can be applied to the screening and control of impurities for the most important risk assessment elements such as Cd, Pb, As, Hg, V, Co, and Ni, as well as for important catalyst elements including Ir, Pt, Ru, Rh, and Pd in pharmaceutical materials. The major benefit of the technique is that it reduces the need for complicated and time-consuming chemical digestion procedures and can be a very useful addition as an initial screening tool to reduce the number of samples that need to be analyzed by ICP-OES or ICP-MS.

References

(1) International Conference on Harmonization, *ICH Q3D Step 4 Guidelines: Guideline for Elemental Impurities*, (ICH, Geneva, Switzerland, 2014).

(2) General Chapter <735> "X-ray Fluorescence Spectrometry" in *United States Pharmacopeia 37–National Formulary 32* (United States Pharmacopeial Convention, Rockville, Maryland, 2015).

(3) General Chapter <232> "Elemental Impurities – Limits" in *United States Pharmacopeia 39–National Formulary 34* (United States Pharmacopeial Convention, Rockville, Maryland, 2016).

(4) General Chapter <233> "Elemental Impurities – Procedures" in *United States Pharmacopeia 39–National Formulary 34* (United States Pharmacopeial Convention, Rockville, Maryland, 2016).

(5) "The Use of EDXRF for Pharmaceutical Material Elemental Impurity Analysis," white paper, Shimadzu Scientific Instruments (2016).

Dan Davis is the Elemental Spectroscopy Product Manager for Shimadzu Scientific Instruments. He received a B.S. degree in Chemistry from Towson State University. He is responsible for managing the elemental spectroscopy products in North and Central America for Shimadzu including: ICP emission systems, atomic absorption systems, X-ray fluorescence and diffraction systems, and total organic carbon analyzers. He has more than 15 years of experience in the industry and contributes to ASTM and Standard Methods through review and submission of analytical methods.

Hiroaki Furukawa is the General Manager of the X-ray and Surface Analysis Business Unit for Shimadzu Corporation, Japan. He received a masters degree in Functional Materials from Niigata University. He is responsible for managing the electron probe microanalyzer systems, X-ray fluorescence and diffraction systems, and scanning probe microscope systems in Japan and overseas for Shimadzu. He has almost 20 years of experience in development and as an application engineer of X-ray products including total reflection X-ray fluorescence, X-ray reflectivity, and X-ray absorption fine structure.

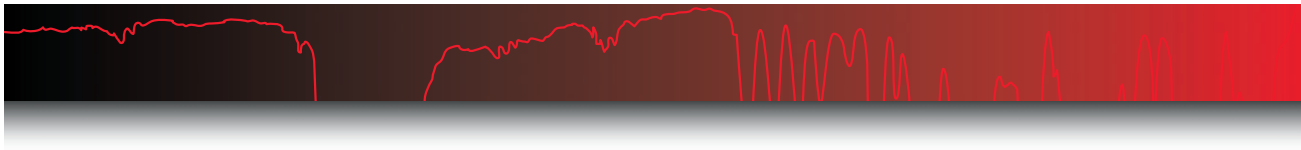

IR Spectral Interpretation Workshop

An IR Spectral Interpretation Potpourri: Carbohydrates and Alkynes

We finish our examination of the infrared (IR) spectroscopy of the C-O bond with a discussion of carbohydrates. These important biological molecules contain both alcohol and ether linkages, making their C-O stretching regions particularly rich and challenging to interpret. To round out this potpourri I've added alkynes, a type of unsaturated functional group for which there wasn't room in earlier columns.

Brian C. Smith

According to *Webster's Collegiate Dictionary* (1), a *potpourri* is "a mixture, especially of unrelated objects, subjects etc." One of the challenges of writing multiple column installments for a magazine is making the topics fit into the space allotted in each issue. More than once in the past there has been a topic that was too short to stand by itself as an installment, but too long to combine with any related topics. Hence the need for the occasional catch-all column like this one, where these orphaned topics can find a home. The reason that this installment is a potpourri is that the topics included here are unrelated to each other. There will be more potpourri columns in the future.

This is also the 14th installment of this workshop, and in the last two and a half years we have covered a lot of territory. The topics covered in potpourri installments will be new to you but are related to things we have discussed before. Therefore, you will learn something new from these columns while exercising some of what you have already learned, hopefully aiding in your learning process.

Carbohydrates

Carbohydrates are an important class of biological compounds including sugars and cellulose. The term was originally coined because their molecular formulas suggested they were "hydrates of carbon" (2), although we now know this is not true. Structurally speaking, carbohydrates contain saturated rings with ether linkages in them, and multiple alcohol groups as shown in Figure 1.

So far in these columns most of the compounds whose spectra have been examined have been synthetic compounds of industrial importance, but of course biochemicals are important too because they allow life on planet earth to exist! In many of the infrared (IR) spectral interpretation training courses I have taught, one of the most frequent questions has been, "Can IR tell the difference between synthetic and natural materials?" The short answer is no. Many of the most important classes of biochemicals, including proteins, fats, carbohydrates, and nucleic acids, are structurally similar to organic compounds and contain the same functional groups as synthetic chemicals. The spectrum of any functional group will be the same regardless of whether it was made in a living cell or a test tube. For example, the spectrum of a methyl group will be pretty much the same whether it is part of an alkane or a protein. Thus, IR spectroscopy is not a good "natural versus synthetic" discriminator.

Table I: Summary of IR peak positions for carbohydrates

Band Position	Assignment
3500–3300	O-H stretches
~2900	Lone C-H stretches
1200–1000	C-O stretches

However, since biochemicals do contain organic functional groups, we can determine their structure by IR spectroscopy the same way we do for synthetic materials.

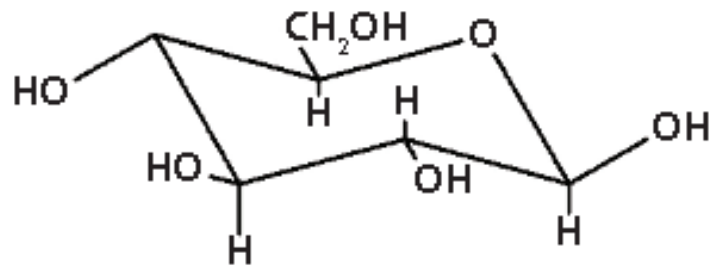

Figure 1: The chemical structure of glucose.

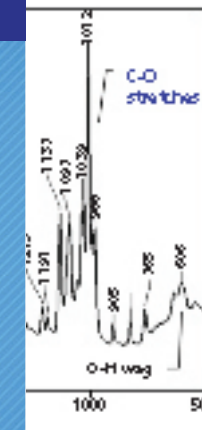

stretches. The seven separate saturated C-O bonds means there will be a lot of C-O stretching peaks between 1200 and 1000 cm^{-1} (going forward assume all peak positions are in cm^{-1} even if not noted). The IR spectrum of glucose is shown in Figure 2.

There is a broad, strong O-H stretching envelope in Figure 2 with two peaks at 3402 and 3318. This is the first time we have seen an O-H stretching peak like this. It means there are two chemically distinct alcohol groups in the molecule with different bond strengths, force constants, and hence peak positions. My small and water's contribution to the -OH stretching peak intensity would also be small. It is no surprise that glucose and many other carbohydrates absorb water from the atmosphere since they contain a lot of -OH groups, are highly polar, and hence are hygroscopic.

Four of the carbons in the glucose ring are structurally similar—each being attached to two other carbons, one oxygen, and one hydrogen, with the oxygens each being part of a secondary alcohol. We will call the situation where there is only one hydrogen attached to a carbon a *lone hydrogen*.

ns in glucose are all
ce will have C-H
00 (2). However,
ot be as intense as
hes since there is
tributing to the
ead of two or three
as is the case for methylene and methyl groups. Saturated lone C-H groups tend to have their stretching peaks around 2900 (7). The oddball fifth carbon in the glucose ring has a primary alcohol group hanging off it that contains a CH_2 group. It is these C-H and CH_2 moieties that are responsible for the small C-H stretching peaks shown in Figure 2 around 2900.

Recall that saturated ethers have a C-O stretching peak from 1140 to 1070, secondary alcohols have one from 1150 to 1075, and in primary alcohols this peak appears between 1075 and 1000 (3–5), making for a poten-

IR Spectral Interpretation Workshop

An IR Spectral Interpretation Potpourri: Carbohydrates and A

We finish our exa
of carbohydrates.
making their C-O
potpourri I've ad
earlier columns.

Brian C. Smith

According to *W*
pourri is "a m
subjects etc."
tiple column installm
ics fit into the space a
in the past there has b
by itself as an installm
related topics. Hence the need for the occasional catch-all column like this one, where these orphaned topics can find a home. The reason that this installment is a potpourri is that the topics included here are unrelated to each other. There will be more potpourri columns in the future.

This is also the 14th installment of this workshop, and in the last two and a half years we have covered a lot of territory. The topics covered in potpourri installments will be new to you but are related to things we have discussed before. Therefore, you will learn something new from these columns while exercising some of what you have already learned, hopefully aiding in your learning process.

Carbohydrates

Carbohydrates are an important class of biological compounds including sugars and cellulose. The term was

pounds of industrial importance, but of course biochemicals are important too because they allow life on planet earth to exist! In many of the infrared (IR) spectral interpretation training courses I have taught, one of the most frequent questions has been, "Can IR tell the difference between synthetic and natural materials?" The short answer is no. Many of the most important classes of biochemicals, including proteins, fats, carbohydrates, and nucleic acids, are structurally similar to organic compounds and contain the same functional groups as synthetic chemicals. The spectrum of any functional group will be the same regardless of whether it was made in a living cell or a test tube. For example, the spectrum of a methyl group will be pretty much the same whether it is part of an alkane or a protein. Thus, IR spectroscopy is not a good "natural versus synthetic" discriminator.

Table I: Summary of IR peak positions for carbohydrates

Band Position	Assignment
3500–3300	O-H stretches
~2900	Lone C-H stretches
1200–1000	C-O stretches

However, since biochemicals do contain organic functional groups, we can determine their structure by IR spectroscopy the same way we do for synthetic materials.

Mono- and Disaccharides

The chemical structure of an important and well known carbohydrate, glucose, is shown in Figure 1.

Glucose is the product of photosynthesis, and is the molecule many animals burn for energy. Note that it is a cyclic six-membered ring with the shape of a distorted hexagon. Glucose is an example of a monosaccharide, meaning it contains one cyclic sugar unit. Five of the vertices of this saturated ring represents a carbon atom, and the ring also contains an oxygen atom attached to two saturated carbons giving a saturated ether linkage. Additionally, there are also five -OH groups, four of which are secondary alcohols and one of which is a primary alcohol. We have studied the spectra of all these functional groups before (3–5). The plethora of hydroxyl groups means that carbohydrates engage extensively in hydrogen bonding and that there will be strong, broad O-H stretches. The seven separate saturated C-O bonds means there will be a lot of C-O stretching peaks between 1200 and 1000 cm^{-1} (going forward assume all peak positions are in cm^{-1} even if not noted). The IR spectrum of glucose is shown in Figure 2.

There is a broad, strong O-H stretching envelope in Figure 2 with two peaks at 3402 and 3318. This is the first time we have seen an O-H stretching peak like this. It means there are two chemically distinct alcohol groups in the molecule with different bond strengths, force constants, and hence peak positions. My guess is that one of the peaks is from the secondary alcohols present, and the other from the primary alcohol present. There is also an O-H wagging peak at 606.

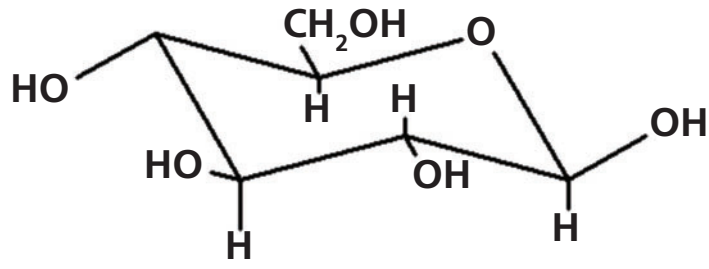

Figure 1: The chemical structure of glucose.

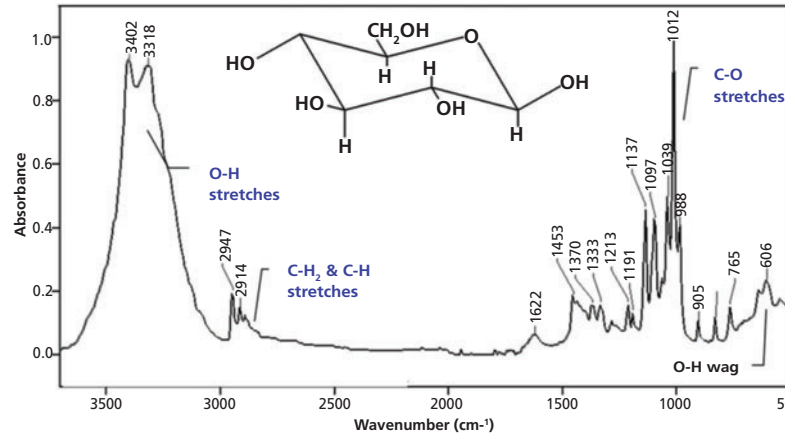

Figure 2: The IR spectrum of glucose, a monosaccharide.

There is a peak at 1622 from adsorbed water, although the peak is small and water's contribution to the -OH stretching peak intensity would also be small. It is no surprise that glucose and many other carbohydrates absorb water from the atmosphere since they contain a lot of -OH groups, are highly polar, and hence are hygroscopic.

Four of the carbons in the glucose ring are structurally similar—each being attached to two other carbons, one oxygen, and one hydrogen, with the oxygens each being part of a secondary alcohol. We will call the situation where there is only one hydrogen attached to a carbon a *lone hydrogen*. The lone hydrogens in glucose are all saturated and hence will have C-H stretches below 3000 (2). However, these peaks will not be as intense as typical C-H stretches since there is only one bond contributing to the peak intensity instead of two or three as is the case for methylene and methyl groups. Saturated lone C-H groups tend to have their stretching peaks around 2900 (7). The oddball fifth carbon in the glucose ring has a primary alcohol group hanging off it that contains a CH_2 group. It is these C-H and CH_2 moieties that are responsible for the small C-H stretching peaks shown in Figure 2 around 2900.

Recall that saturated ethers have a C-O stretching peak from 1140 to 1070, secondary alcohols have one from 1150 to 1075, and in primary alcohols this peak appears between 1075 and 1000 (3–5), making for a poten-

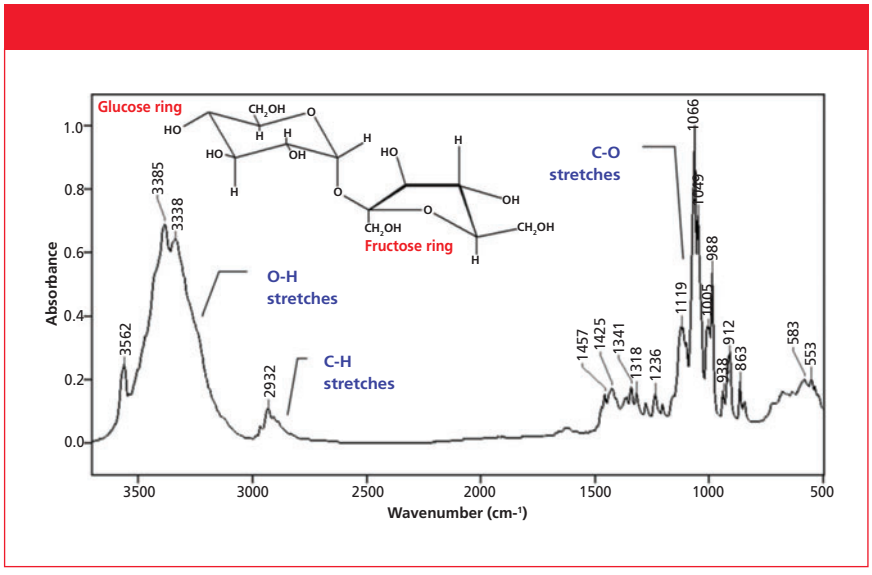

Figure 3: The IR spectrum of sucrose (table sugar), a disaccharide.

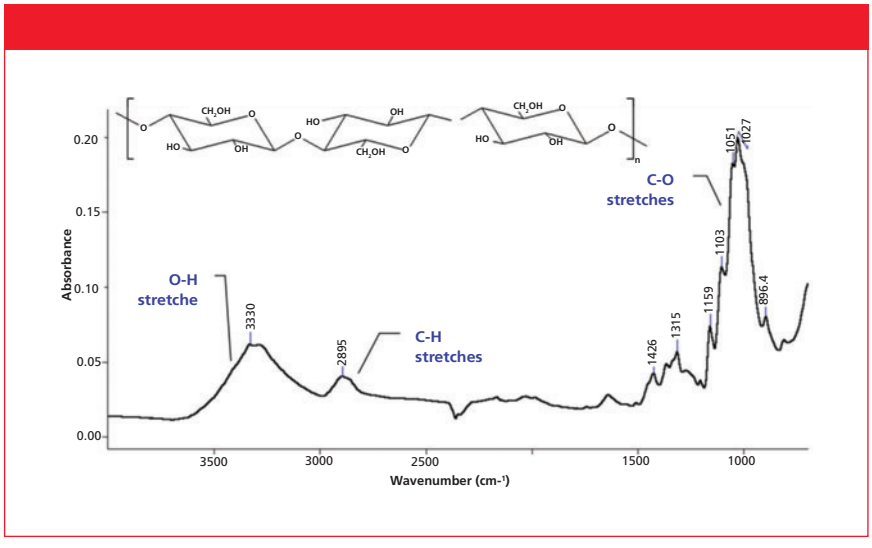

Figure 4: The IR spectrum of cellulose, a polysaccharide.

tially complex C-O stretching region. As can be seen in Figure 2 there are four peaks in this region. This C-O stretching peak region complexity is typical of carbohydrates, and makes it difficult to assign the C-O stretching peaks of these molecules exactly.

The IR spectrum of a disaccharide, sucrose, otherwise known as table sugar, is shown in Figure 3.

Sucrose is a disaccharide because it contains two sugar rings. It consists of a glucose ring attached via a saturated ether linkage to a five-membered fructose ring as noted in Figure 3. Fructose gets its name from the fact that it is a sugar found in fruit (2). Note in the spectrum that there are multiple O-H and C-O stretching peaks, even more so than in the spectrum of glucose. Many carbohydrates consist of multiple sugar rings connected by ether linkages. As these molecules get bigger there are many more types of O-H and C-O bonds, hence the increase in spectral complexity. Also note in the spectrum of sucrose that the C-H stretch and O-H wag peaks have turned into shapeless blobs thanks to spectral complexity and hydrogen bonding.

Polysaccharides

Polysaccharides are polymeric carbohydrates consisting of many sugar units strung together. Perhaps the most common polysaccharide is cellulose, whose IR spectrum is shown in Figure 4.

Cellulose is found in the cell walls of plants and is found in our every day lives as wood, paper, and cotton. In fact, the spectrum in Figure 4 is of a paper towel. The cellulose molecule is a series of glucose units stitched together by saturated ether linkages. There is so much hydrogen bonding in cellulose that the complex O-H stretching peak patterns we saw in glucose and fructose are gone, replaced by a broad blob. The C-H stretches are similarly blobby, and the C-O stretching region is best characterized as an envelope with any number of shoulder peaks on top of it.

Notice then as we proceeded from mono- to di- to polysaccharides the spectra got more complex because of the many types of O-H and C-O bonds and eventually became so complex that the peaks overlapped enough to form blobs. Hydrogen bonding also helped increase spectral band broadening. The spectra of carbohydrates then are characterized by multiple O-H stretches and multiple C-O stretches. This information is summarized in Table I.

Alkynes

In past columns (10,11) we discussed unsaturated carbons and looked at the spectra of two families of unsaturated hydrocarbons, substituted benzene rings and alkenes. I left out one last family from the discussion, alkynes. Alkynes contain the C≡C structural unit, properly called a carbon-carbon triple bond. These bonds are unsaturated because they can be hydrogenated to form saturated compounds just like aromatic rings and alkenes (2). The two varieties of alkynes, monosubstituted and disubstituted, are shown in Figure 5. The "R-" symbols in Figure 5 represent nonhydrogen substituent atoms.

A monosubstituted alkyne has one hydrogen and one R-group attached, and a disubstituted alkyne has no hydrogens and two R-groups attached. The simplest alkyne with the chemical formula C_2H_2, or H-C≡C-H, is called acetylene. Some-

Figure 5: Left: the structure of a monosubstituted alkyne. Right: the structure of a disubstituted alkyne.

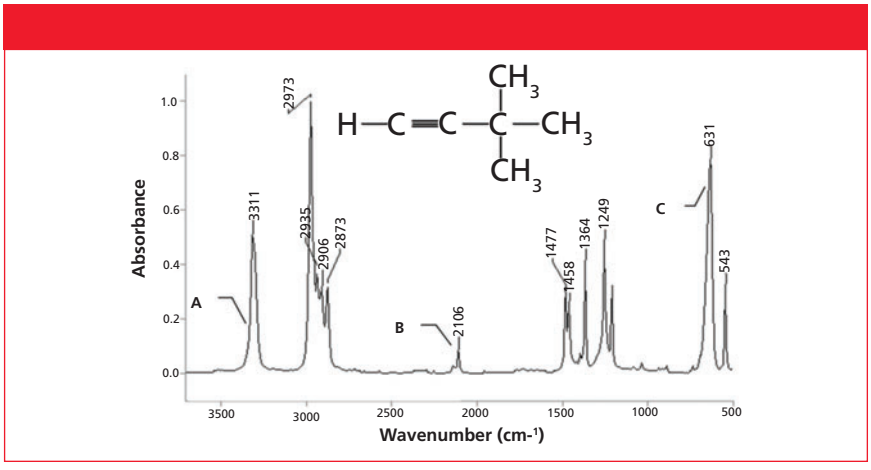

Figure 6: The IR spectrum of 3,3-dimethyl-1-butyne (or *tert*-butyl acetylene), a monosubstituted alkyne.

Table II: Peak assignments for spectrum shown in Figure 5		
A	3311	≡C-H stretch
B	2106	C≡C stretch
C	631	C-H wag

times alkynes are named as acetylene derivatives. We can distinguish the two types of alkynes from each other using IR spectroscopy. The IR spectrum of a monosubstituted alkyne, 3,3-dimethyl-1-butyne (or *tert*-butyl acetylene) is shown in Figure 6, and its relevant peak assignments are shown in Table II.

As we read the spectrum from left to right the first thing we encounter is an intense, relatively sharp peak labeled A at 3311. We have seen in the past (3,4) that O-H stretches fall in this same region. However, recall that these peaks are widened by hydrogen bonding. There is no hydrogen bonding in alkynes, hence the peak at 3311 is narrow and cannot be from an O-H bond. It is in fact the C-H stretch of the hydrogen attached directly to the C≡C group, and this peak generally falls from 3350 to 3250 for monosubstituted alkynes. This is far and away the highest wavenumber C-H stretch we have seen yet and may ever see. Its unique position and sharpness set it apart and make it a great monosubstituted alkyne group wavenumber. The H-C≡C group also has a C-H wag, shown as a big peak labeled C at 631 in Figure 6. This is also an excellent group wavenumber because of its intensity, sharpness, and low peak position. This peak can be found generally from 700 to 600 for monosubstituted alkynes. O-H wags also show up in this region (3,4), but again the sharpness of this peak means it is not from an OH group. The spectra of monosubstituted alkynes then have two sharp, intense peaks at high and low wavenumber, in a sense bookending the spectrum.

The C≡C linkage in monosubstituted alkynes has a stretching peak between 2140 and 2100, which is shown in Figure 6 labeled B at 2106. This is a very unusual peak position, which should make this peak a useful group wavenumber. However, like the C=C stretch of alkenes (11) this peak has variable intensity and hence limited utility because it may be in-

Quiz Section: Answer to the May Quiz and a New Interpretation Challenge

The Last Quiz

The spectrum of the last column's spectral interpretation problem is shown in Figure *i*. Recall (8) that an unknown IR spectrum should be read from left to right like a sentence in a book. The peaks we come to first are a set of four just below 3000. Hopefully by now you recognize these as saturated C-H stretches, and the fact that there are four peaks means there are both methyl and methylene groups present in the molecule (8). The lack of C-H stretches above 3000 means all the carbons in this molecule are saturated. Using the peak positions discussed previously (6), we can identify the peak at 2962 as a methyl asymmetric stretch, the one at 2934 as a methylene asymmetric stretch, and 2871 as a methyl symmetric stretch. When there are four saturated C-H stretching peaks like this the last peak is usually the CH_2 symmetric stretch at 2855 ± 10. However, there is no peak in this range; the last C-H stretching peak is at 2829, a topic we will come back to. Since there are methyl groups there should also be an umbrella mode peak, which is clearly seen at 1386. There is a methylene C-H stretching peak, but there is no CH_2 rock peak at 720, indicating that whatever alkyl chains are present, none of them have more than four CH_2s in a row.

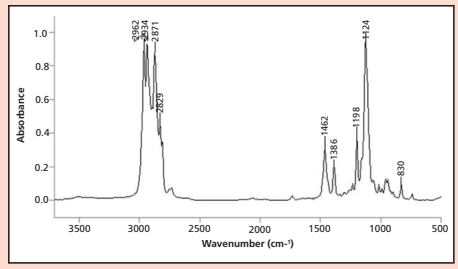

Figure *i*: The problem IR spectrum from the last column.

The dominant peak at low wavenumber in this spectrum is at 1124, which has the proper intensity and position to be a C-O stretch. Now recall that both alcohols and ethers can have an intense peak in this region (3–5). However, there is no broad, strong O-H stretch near 3350 in this spectrum, which means there is no alcohol functional group present. This means that the C-O stretch is most likely from an ether, since we have already established that all the carbons are saturated, it must be a saturated ether. This functional group displays its C-O stretch from 1140 to 1070 (5), so the peak at 1124 is properly assigned as a saturated ether C-O stretch, or more correctly the asymmetric C-O-C stretch. The symmetric C-O-C stretch is found at 830. Since we know we have a saturated ether the C-H stretching peak at 2829 makes sense, it is the asymmetric C-H stretch of a methoxy (-O-CH_3) group (5). This is very useful information; a saturated ether has two different substituents attached to the ether oxygen, and courtesy of the peak at 2829 we now know one of the substituents is a methyl group.

The last task then is to determine the structure of the second substituent on the ether oxygen. We know we have methyl and methylene groups so this is likely an alkyl chain, and we also know it is short because of the lack of a peak at 720. Another tool we can use to estimate alkyl chain length and the CH_2/CH_3 ratio is the relative intensity of the methyl and methylene asymmetric stretches (8). The two relevant peaks here are at 2962 and 2934 and they have the same height, which means that the CH_2/CH_3 ratio is two or more. This eliminates the CH_3-CH_2 (ethyl) group as a substituent since its CH_2/CH_3 ratio is one. Recall that there are no alkyl chains present with more than four CH_2 groups in a row, and we've eliminated the ethyl group, so the only possible alkyl chains left are the propyl group (CH_3-CH_2-CH_2-) with two CH_2 groups in a row and the butyl group (CH_3-CH_2-CH_2-CH_2-) with three methylenes in a row. Unfortunately, we have pushed this analysis as far as we can. As we have seen in previous interpretation workshops, it is not always possible to determine the exact length of an alkyl chain from an IR spectrum by itself. At this point, spectral atlases or library searching would help distinguish between the two possibilities. Remember that armed only with the spectrum we narrowed down the possibilities from the almost 10 million organic compounds known to man (9) to two, not a bad day's work.

It turns out the alkyl chain in question is butyl, and the compound is methyl butyl ether, $C_5H_{12}O$. Its chemical structure is shown in Figure *ii*, and Table *i* shows its proper peak assignments.

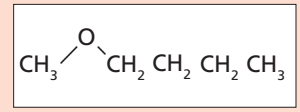

Figure *ii*: The chemical structure of methyl butyl ether, the answer to last installments spectral interpretation column.

Table *i*: Correct peak assignments for problem spectrum seen in Figure *i*

Peak	Assignment
2962	CH_3 asymmetric stretch
2934	CH_2 asymmetric stretch
2871	CH_3 symmetric stretch
2829	CH_3-O methoxy symmetric stretch
1386	CH_3 umbrella mode
1124	Ether asymmetric C-C-O ("C-O") stretch
830	Symmetric C-C-O stretch

New Quiz

Using what you have learned from this and other columns, do your best to assign the peaks in this spectrum, determine the functional groups present, and determine the chemical structure of the molecule that gave rise to this spectrum. Ignore the peaks with an x through them.

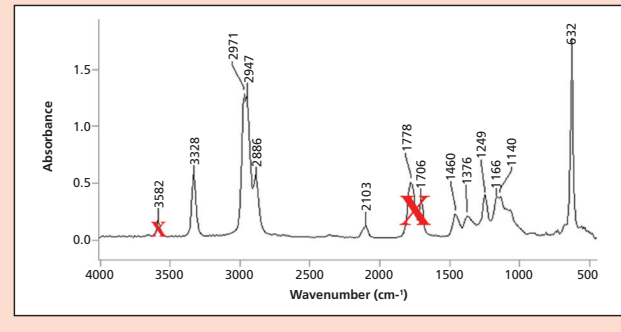

Figure *iii*: The IR spectrum of a gas (ignore the peaks with X's through them).

thermo scientific

What did you do today?

Whether you're discovering new materials, solving analytical problems or assuring product quality, your spectrometer needs to deliver the definitive answers you're looking for — fast! Thermo Fisher Scientific goes beyond your expectations with a full line of FTIR, NIR and Raman spectroscopy systems, to help you move from sample to answer . . . faster than ever before.

The Thermo Scientific™ Nicolet™ iS50 FTIR Spectrometer is your all-in-one materials analysis workstation. With simple one-touch operation and fully-integrated diamond ATR, the Nicolet iS50 gives your lab the productivity you need today and the capabilities you need tomorrow.

Discover. Solve. Assure. **thermofisher.com/solve-is50**

ThermoFisher SCIENTIFIC

tense, weak, or nonexistent depending on the molecule. Recall that one of the things that determines peak intensity is the change in dipole moment with respect to bond length (dμ/d*x*) for a vibration (8). For a monosubstituted alkyne with a polar substituent dμ/d*x* will be large and the C≡C stretching peak will be large. For a monosubstituted alkyne with a nonpolar substituent like *tert*-butyl acetylene, dμ/d*x* will be small and hence the peak intensity will be small as seen in Figure 6. For a symmetrically substituted alkyne such as acetylene (H-C≡C-H) dμ/d*x* for the triple bond stretch is zero and there is no IR peak due to C≡C stretching. The unreliable appearance of this peak makes it a poor group wavenumber. Again, the best peaks to identify a monosubstituted alkyne are the H-C≡C stretch and wag.

A disubstituted alkyne has two non-hydrogen substituents attached, such as dimethyl acetylene, CH_3-C≡C-CH_3. Since there are no hydrogens attached to the triple bond, disubstituted alkynes do not have a H-C≡C stretching or bending vibration. Disubstituted alkynes do have a C≡C stretching peak that falls between 2260 and 2190, and this peak can be used to distinguish disubstituted from monosubstituted alkynes. However, just like for monosubstituted alkynes, the C≡C stretch is also an unreliable group wavenumber for the same reasons. For a symmetrically substituted disubstituted alkyne like dimethyl acetylene there are no H-C≡C peaks, and since dμ/d*x* for the C≡C stretch is zero there is no triple bond stretching peak. Symmetrically substituted alkynes then are one of the rare organic functional groups that have no useful IR group wavenumbers, and their presence in a sample must be detected by means other than IR spectroscopy.

Conclusion

In this first IR spectral interpretation potpourri we have looked at the spectra of two dissimilar molecules, carbohydrates and alkynes. Carbohydrates contain many different types of O-H and C-O bonds, and hence have complex O-H stretching and C-O stretching regions from 3500 to 3300 and 1200 to 1000, respectively.

Alkynes contain C≡C bonds and come in mono- and disubstituted forms. Mono-substituted alkynes contain a unique H-C≡C group with a sharp, intense high wavenumber C-H stretch, and a sharp, intense, low wavenumber C-H wag. C≡C stretching peaks appear uniquely around 2200 but suffer from variable intensity, making them a questionable group wavenumber. This is the only diagnostic peak that disubstituted alkynes possess, sometimes making them difficult to detect.

References

(1) *Webster's Collegiate Dictionary* (G.C. Merriam, Cambridge, Massachusetts, 1946).
(2) A. Streitwieser and C. Heathcock, *Introduction to Organic Chemistry* (Macmillan, New York, 1976).
(3) B.C. Smith, *Spectroscopy* **32**(1), 14–21 (2017).
(4) B.C. Smith, *Spectroscopy* **32**(4), 19–23 (2017).
(5) B.C. Smith, *Spectroscopy* **32**(5), 22–26 (2017).
(6) B.C. Smith, *Spectroscopy* **30**(4), 18–23 (2015).
(7) B.C. Smith, *Infrared Spectral Interpretation: A Systematic Approach* (CRC Press, Boca Raton, Florida, 1999).
(8) B.C. Smith, *Spectroscopy* **30**(9), 40–45 (2015).
(9) Beilstein Electronic Organic Chemical Database, contents as of 6/2017.
(10) B.C. Smith, *Spectroscopy* **31**(3), 34–37 (2016).
(11) B.C. Smith, *Spectroscopy* **31**(11), 28–34 (2016).

Brian C. Smith, PhD, is the West Coast Business Development Manager for CAMO Software, a company that sells chemometric, multivariate analysis, and process control software. Before joining CAMO, Dr. Smith ran his own FT-IR training and consulting business for more than 20 years. Dr. Smith has written three books on infrared spectroscopy: *Fundamentals of FTIR* and *Infrared Spectral Interpretation*, both published by CRC Press, and *Quantitative Spectroscopy: Theory and Practice* published by Academic Press. He can be reached at: SpectroscopyEdit@UBM.com

Trends in X-Ray Techniques

In advance of the Denver X-Ray Conference, we asked leading scientists who will be speaking at the conference about current trends and advances in X-ray fluorescence and X-ray diffraction. Here, these investigators discuss their work to advance these techniques and the sample preparation for such analyses, in areas such as photonics for telecommunications, steel structures, metals in pharmaceuticals, and imaging.

Simplifying Metal Analyses in Pharmaceutical Labs with XRF

Sharla Wood

Metal catalysts may be found at multiple points along the synthetic route of a drug product, including starting materials, intermediates, excipients, and in the synthesis of the active pharmaceutical ingredient (API). Although the procedures in the *International Conference on Harmonisation* (*ICH*)-*Q3D Elemental Impurities* and *United States Pharmacopeia* (*USP*) chapters *<232> Elemental Impurities - Limits* and *<233> Elemental Impurities* (1–3) govern elemental impurities in drug products, analyses of metal concentrations in starting materials, intermediates, in-process materials, and during process optimization of API synthesis are also beneficial. Since the primary goal of providing life-saving drugs to patients more quickly is often the driving force behind many decisions in the pharmaceutical development process, alternatives to traditional metal analysis methods that can provide more timely results with less required skill are desirable.

Traditionally, metal analysis in pharmaceuticals is conducted using flame- and plasma-based techniques, including flame and graphite furnace atomic absorption spectroscopy, inductively coupled plasma–mass spectrometry (ICP-MS), and inductively coupled plasma–optical emission spectroscopy (ICP-OES). These techniques offer sensitivity, selectivity, and precision; however, they often require lengthy sample preparation and trained analysts, regardless of the stage of development. Time is an important consideration during the pharmaceutical development process, and often a quick estimate of metal concentration is all that is necessary when deciding the next step in the optimization of a synthetic process. A wish list for an alternative technique includes fast and simple method development, the potential for open access and sample flexibility (including phase and sample size), while still maintaining the required sensitivity for screening of metal content and for trending data. X-ray fluorescence (XRF) provides an alternative approach to determine elemental content. Although portable XRF may not afford the same level of sensitivity as ICP-MS or ICP-OES, it is relatively inexpensive, is easy for an untrained individual to use, requires little-to-no sample preparation, and is nondestructive.

A portable XRF system was provided for use in process chemistry laboratories to enable rapid screening of metal catalyst content to isolate samples of high metal concentrations and determine trends in metal concentrations during metal catalyst removal processes (4). Through the use of XRF, synthetic chemists were able to generate data in their laboratory within minutes to aid in the design of future experiments. Sample quantity is often limited during the development process; the nondestructive behavior of XRF afforded the recovery of samples after analysis for use in subsequent experiments. Moreover, the volume of samples submitted for ICP analysis was greatly reduced, saving both instrument and personnel time, reducing consumable and reagent costs, and decreasing the potential for instrument contamination by samples with high metal concentrations. Since the deployment of this XRF system, more than 900 samples were analyzed by this XRF screening method, saving approximately two months of development time.

Portable XRF spectroscopy has proven useful in the screening of effective metal catalyst scavengers during the pharmaceutical development process and for metal analysis at in-process control steps during the synthesis of a pharmaceutical product, results from which have been used in critical decisions. This technique has also shown to be invaluable in foreign matter investigations, metal analysis of excipients and vendor-sourced materials, as well as materials that are not easily solubilized, and in the analysis of in-process control samples during the synthetic process of APIs.

References

(1) International Conference on Harmonization, *ICH Q3D, Guideline for Elemental Impurities*, (ICH, Geneva, Switzerland, 2014, http://www.ich.org/fileadmin/Public_Web_Site/ICH_Products/Guidelines/Quality/Q3D/Q3D_Step_4.pdf).

(2) General Chapter <232> "Elemental Impurities - Limits" in *United States Pharmacopeia 39–National Formulary 34* (United States Pharmacopeial Convention, Rockville, Maryland, http://www.usp.org/sites/default/files/usp_pdf/

40 years of Products for *Your* Imagination

New in-house manufacturing = The highest performing detectors available

The True State-of-the-Art

NEW

Ultra High Performance FAST SDD®

Lower noise » Better resolution down to 122 eV

Lower leakage current » Higher temperature operation (save battery life)

Better charge collection » Better photo peak shape (no tailing)

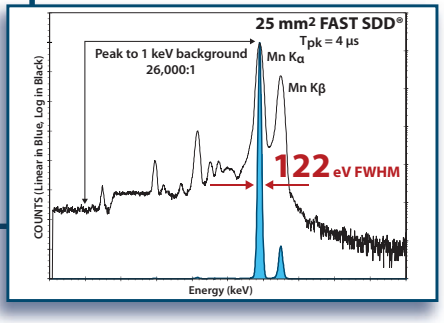

NEW

Large Area FAST SDD®

- 70 mm² active, collimated to 50 mm²
- 123 eV FWHM, 42 eV at C K_α line
- Count rates > 2,000,000 CPS
- Same pinout, interface as 25 mm²

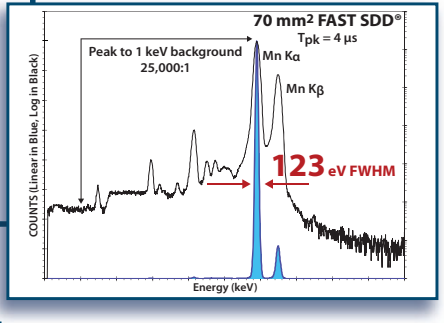

NEW

Improved SDD

- 125 eV FWHM resolution @ 5.9 keV
- High Peak-to-Background Ratio – 20,000:1
- 25 mm² – collimated to 17 mm²
- 500 µm thick

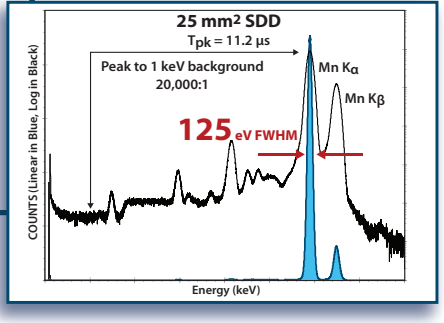

NEW

Improved Si-PIN

- 139 eV FWHM resolution @ 5.9 keV
- 6, 13 or 25 mm²
- High Peak-to-Background Ratio – 19,000:1

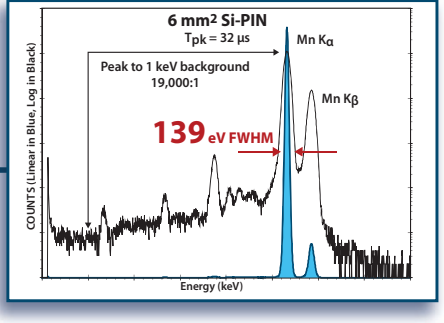

www.amptek.com

State-of-the-Art X-Ray Solutions

•FAST SDD® •SDD •Si-PIN

The best detector for optimal results

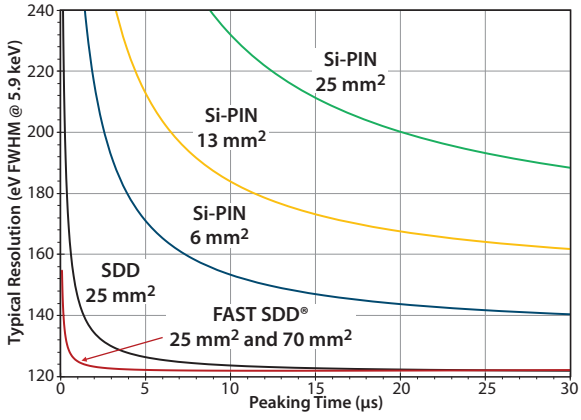

FAST SDD® Detector

>2,000,000 CPS and 122 eV FWHM Resolution

Options:

- 25 mm^2 collimated to 17 mm^2
- 70 mm^2 collimated to 50 mm^2
- Windows: Be (0.5 mil) 12.5 µm, or C Series (Si_3N_4)
- TO-8 package fits all Amptek configurations

Configurations to meet your needs

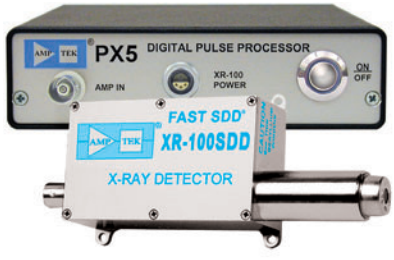

XR-100 and PX5 Digital Pulse Processor

X-123 Complete X-Ray Spectrometer

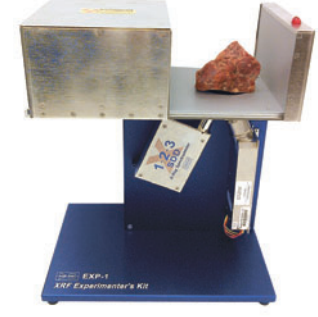

XRF Experimenters Kit

OEM Configurations

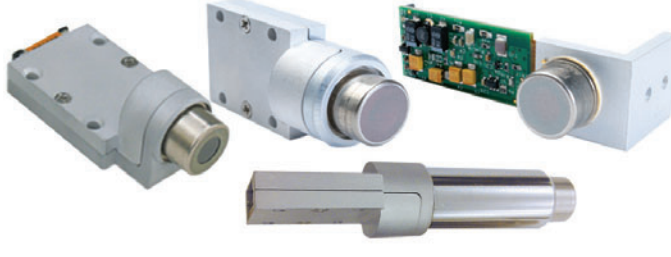

A sample of detectors with preamplifiers and heat sinks

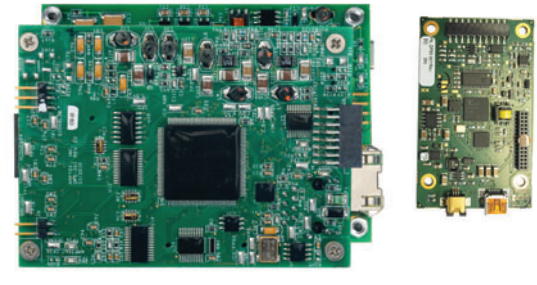

Digital Pulse Processors and Power Supplies

AMP TEK®

OEM's #1 Choice For XRF

AMETEK®
MATERIALS ANALYSIS DIVISION

EN/USPNF/key-issues/c232-usp-39.pdf).

(3) General Chapter <233> Elemental Impurities - Procedures" in second supplement to *United States Pharmacopeia 38–National Formulary 33* (United States Pharmacopeial Convention, Rockville, Maryland, http://www.usp.org/sites/default/files/usp_pdf/EN/USPNF/key-issues/c233.pdf).

(4) N. Lewen et al., *Org. Process Res. Dev.* **19**(12), 2039–2044 (2015).

Sharla Wood is a Research Investigator II at Bristol-Myers Squibb in Global Product Development and Supply - Chemical and Synthetic Development in New Brunswick, New Jersey.

Analysis of Beverages by Total Reflection X-ray Fluorescence

Martina Schmeling

Total reflection X-ray fluorescence spectrometry (TXRF) is a well established and versatile multielement trace analytical method. (1). Its ease of use and low detection limits make it an ideal tool for routine analysis of samples ranging from liquids and solids to biological tissues. The project presented in this short article was inspired by undergraduate research experience and showcases TXRF as an undergraduate teaching and research tool. When exposing undergraduate students to research one has to take into account the lack of laboratory experience of the student, in addition the project should spark and retain the interest of the student, and also maintain a high research standard. With this in mind, the subject of study were common beverages. Beverages such as juices are recommended as a means of delivering essential nutrients and trace elements to children and adults alike. Many of them are fortified and most are processed to remove unwanted residues and pulp or are reconstituted from concentrate. We purchased three common fruit juices—apple juice, cranberry juice, orange juice—and one bottle of lemonade for this study and compared their metal content to water obtained from a drinking fountain at the university. All fruit juices were pulp free and none of the beverages were from concentrate. Table I lists the name, origin, and daily values of the beverages stated on the label.

Two sample preparation methods were compared with each other to examine the difference in trace metal content between the liquid part of the juice and the solid–liquid mixture that includes plant fibers. For the liquid-only element content, a 5-mL aliquot of the purchased beverages was centrifuged at 9000 rpm for 10 min and 1 mL of the supernatant was analyzed. For the solid–liquid mixture, a 1-mL aliquot of the beverages was diluted with the same amount of ultrapure water after shaking the bottle vigorously and then analyzed. Drinking fountain water was analyzed directly. For all samples gallium was used as the internal standard.

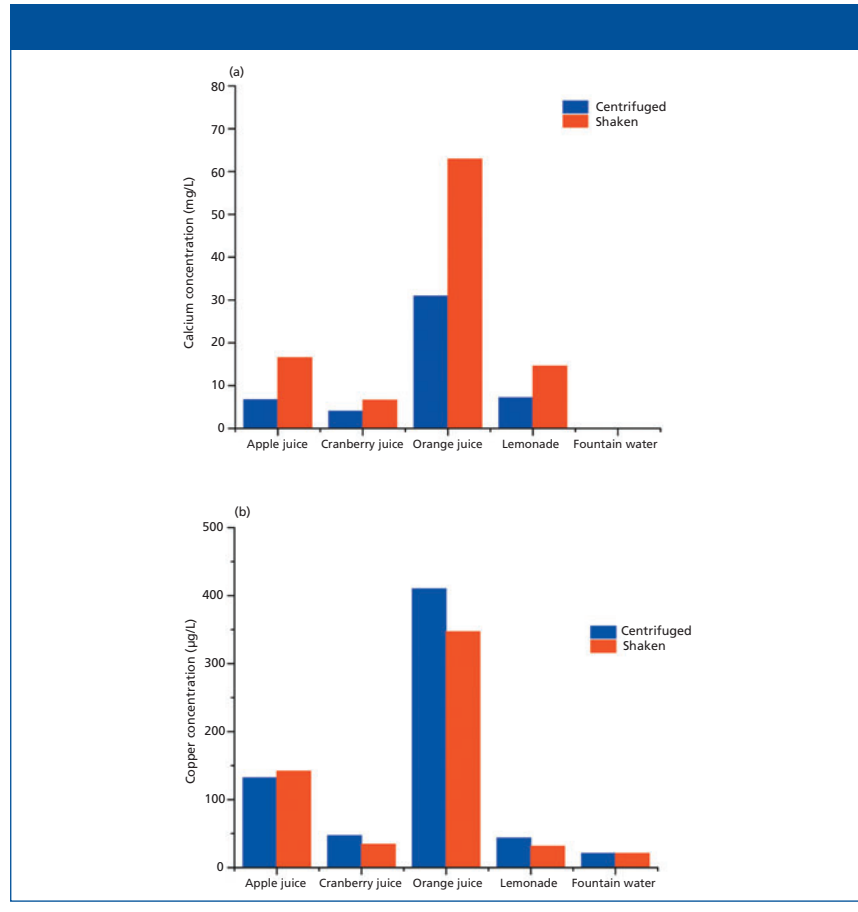

Figure 1: (a) Calcium and (b) copper concentrations in different beverages. The blue bars show the concentrations of the supernatant after centrifugation and the red bars the concentrations of the shaken beverage.

It was found that each purchased beverage contained a suite of common metals, with potassium and calcium having the highest concentrations and manganese, iron, copper, zinc, rubidium, and strontium present as traces. The concentrations of all detected metals varied not only between beverages, but also between the methods of preparation substantially. Drinking fountain water contained much lower concentrations of potassium and calcium, but comparable concentrations for the other metals were detected. This is not surprising because the plant tissue is enriched with potassium and calcium.

Figure 1 shows the concentrations of calcium (Figure 1a) and copper (Figure 1b) for all samples. Please note that the calcium concentrations are expressed in units of milligrams per liter and the copper concentrations in micrograms per liter. The fountain water concentration of calcium was a factor of 1000 smaller than for the other beverages. When calculated for the 340-mL bottle content and compared to daily intake

values, the freshly pressed apple and orange juices delivered more calcium and copper. In fact, the copper amount delivered by one 340-mL bottle of orange juice is about a quarter of the daily recommended value for children and 10% for adults. (2). The juice that contributed substantially to daily intake values was 100% orange juice and only when the solids or pulp were included in the drink. All other beverages had only marginal daily amounts of the metals detectable by TXRF.

Table I: Beverage information as shown on the back label. All beverages were not from concentrate and the nutrition facts are listed for the bottle content of 340 mL.

Nutrition Facts	Apple Juice	Cranberry Juice	Orange Juice	Lemonade
Content	100% juice	27% juice, filtered water, sugar, natural flavors	100% juice	11% lemon juice, filtered water, cane sugar, natural flavor
Fat	0	0	0	0
Sugars	40 g	48 g	33 g	40 g
Total carbohydrates	43 g (14% DV)	49 g (16% DV)	37 g (12% DV)	43 g (14% DV)
Na	5 mg	25 mg	—	20 mg
K	340 mg (10% DV)	—	640 mg (18% DV)	—

References

(1) R. Klockenkämper and A. von Bohlen, *Total Reflection X-ray Fluorescence Analysis and Related Methods*, 2nd Edition (Wiley and Sons, Hoboken, New Jersey, 2015).

(2) Institute of Medicine, *Dietary Reference Intakes for Vitamin A, Vitamin K, Arsenic, Boron, Chromium, Copper, Iodine, Iron, Manganese, Molybdenum, Nickel, Silicon, Vanadium, and Zinc* (The National Academies Press, Washington, DC, 2001) https://doi.org/10.17226/10026.

Martina Schmeling is an Associate Professor and Graduate Program Director with the Department of Chemistry and Biochemistry at Loyola University Chicago in Chicago, Illinois.

In Situ XRD Studies of Microstructural Changes in Steel

M. Witte and I. Janssen

With in situ X-ray diffraction (XRD), microstructure changes in steel can be investigated at elevated temperatures. The method collects large amounts of data in a short time from a single sample, which reduces experimental effort and possible deviations caused by sample preparation. Such experiments can be used to study and optimize annealing treatments of advanced steel grades.

A Bruker D8 Discover X-ray diffractometer with a Vantec2000 area detector was equipped with a DHS1100 commercial heating stage from Anton Paar. With the large angular coverage of the area detector, fast measurements are possible with a temporal resolution of down to 3 s. The heating stage is enclosed by a graphite dome that can be filled with different annealing atmospheres. After preliminary testing of different atmospheres (air, vacuum of 10^{-2} mbar, helium, and nitrogen) a mixture of helium with 3% hydrogen was chosen because it offers high thermal conductivity and the hydrogen content prevents surface oxidation but does not damage the oxide heating plate. The maximum temperature of the heating stage is 1100 °C and the maximal heating rate is 400 °C/min.

In the following section, two examples of in situ XRD measurements of steel are presented.

Recrystallization and Phase Transformation

Recrystallization and recovery are softening processes that are driven by the reduction of dislocation density

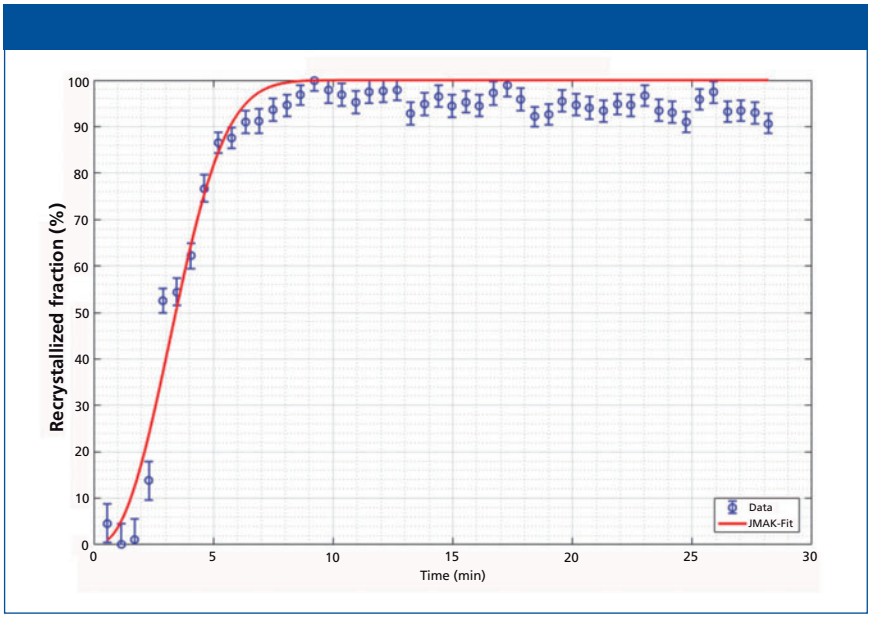

Figure 1: Recrystallized fraction of a dual-phase steel annealed at 700 °C. The fractions are derived from the width of the {110} Bragg reflex measured with in situ XRD.

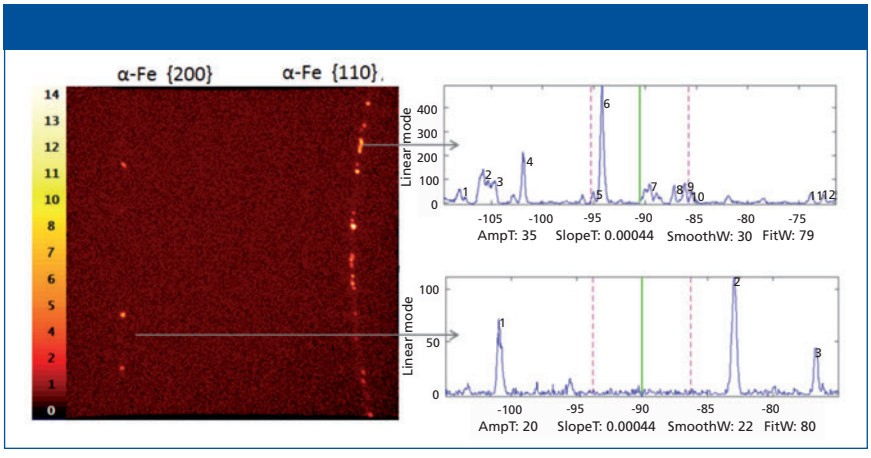

Figure 2: Example of a 2D X-ray detector image of coarse-grained steel. On the right-hand side the result of the automatic spot detection for the {110} and {200} reflexes is given.

of deformed materials. A reduction in dislocation density can be directly determined with in situ XRD by the reduction of X-ray peak widths (1). In the current case, a cold-rolled dual-phase steel was heated to temperatures between 700 °C and 800 °C with a heating rate of 200 °C/min. To derive a recrystallized fraction, the change of the {110}- and {200}-peak widths was normalized. The trend of this recrystallized fraction with annealing time could be fitted with the Johnson-Mehl-Avrami-Kolmogorov (JMAK) function with a high degree of confidence (Figure 1). Hence, the thermodynamic parameters that describe the recrystallization kinetic of this steel could be derived from only three samples within a few hours.

If the same dual-phase steel was heated to higher temperatures, phase transformation sets in. Unfortunately, a decarburization of the sample surface occurred to a larger extent than the X-ray penetration depth. Because the reduction of carbon content increases the transformation temperature considerably, no reliable results of transformation kinetics could be gained. Most likely the decarburization was caused by residual moisture in the annealing atmosphere. In the future, additional gas cleaning filters will be installed to prevent this decarburization effect.

Transformation Textures and Grain Size

To investigate changes of the crystallographic texture caused by the transformation from the low-temperature α-Fe phase (bcc) into the high-temperature γ-Fe phase (fcc), a sample of a bainitic steel was repeatedly heated up to 1000 °C and cooled down to room temperature. As the heating stage is small and flexible enough to allow rotations and tilts of the sample stage, it was possible to measure the complete texture of the sample. For this, three incomplete pole figures were measured at 1000 °C and at room temperature within 20 min. In accordance with other studies (2), a weakening of texture by subsequent phase transformations was observed. Thus, with oscillations around the phase transformation temperature a virtually texture-free microstructure can be obtained. As crystallographic texture is the main cause of plastic anisotropy, such annealing treatments could be used for increasing the isotropy of steels.

Furthermore, the grain size of the same bainitic steel could also be measured in the high-temperature phase. The aim of this investigation was to determine if the prior γ-Fe grain size can be measured by in situ XRD. For coarse-grained materials the Bragg reflexes recorded by an area detector are not smooth cones anymore, but are spotty. Every spot along the Bragg cone originates from a single grain, and from the number of these spots within a certain angular range, the size of the grains can be calculated (Figure 2) (3). For this calculation the interaction volume of the X-ray beam with the sample has to be known or, as in our case, a calibration with a known standard can be applied. Because the penetration depth of the X-ray was approximately 10 µm and thus smaller than the mean grain size, a two-dimensional (2D) approach was derived. In addition to the mean grain size, the grain size distribution can also be determined because the intensity of each spot along the Bragg cone corresponds to the respective size of a certain grain. From a reconstruction of the prior γ-Fe grain structure from electron backscatter diffraction data (EBSD) data, the prior γ-Fe grain size of the investigated bainitic steel was determined to be larger than 500 µm, while

after the reverse transformation into the high temperature γ-phase a grain size of only ~25 µm was determined by in situ XRD. From this result, it follows that the prior γ-Fe grain size is not restored after a reverse transformation into γ-Fe because the change of crystal structure that occurs is diffusive and not displacive (like γ-Fe → martensite or bainite).

In conclusion, in situ XRD measurements are a versatile tool to observe and understand microstructural changes in steel and optimize annealing treatments.

References

(1) G. Williamson and W. Hall, *Acta Metall.* **1,** 22–31 (1953).
(2) G. Brückner and G. Gottstein, *ISIJ Int.* **41,** 468–477 (2001).
(3) B.B He, *Two-Dimensional X-ray Diffraction* (John Wiley & Sons, Hoboken, New Jersey, 2009).

M. Witte is with Salzgitter Mannesmann Forschung GmbH in Salzgitter, Germany. **I. Janssen** is with the Department of Crystallography at Georg-August University Göttingen in Göttingen, Germany.

High-Resolution X-ray Emission Spectroscopy Without a Synchrotron

Kathryn McIntosh, George J. Havrilla, Mark Croce, Rachel Huber, David Podlesak, Michael Rabin, Fernando Vila, Matthew Carpenter, and Robin Cantor

Transition-edge sensor (TES) microcalorimeter detectors are capable of high-resolution X-ray emission spectroscopy (XES) that rivals X-ray absorption near edge structure (XANES) spectroscopic probes found only within the confines of synchrotrons. Commercial microcalorimeters offer a spectral resolution of around 5–7 eV, which is comparable to that provided by wavelength dispersive X-ray fluorescence (WDXRF) instruments yet provides the full spectra of the material of interest, not merely a single element, thereby surpassing WDXRF capabilities.

The bonding of carbon is predicated on the sp^2–sp^3 orbitals. The peak position of the carbon Kα peak, as well as the peak shape, provides information about the bonding of the carbon atoms. In a paper we are presenting at the 2017 Denver X-ray Conference (1), we report the measurement of the carbon Kα peak around 282 eV for several materials of interest, including amorphous carbon, nanodiamond, and graphite, since all three have different carbon forms and sp^2–sp^3 bonding ratios. In addition, a soot specimen from a contained detonation of explosive material was measured to determine the carbon species formed from the detonation. A high-resolution microcalorimeter mounted on a scanning electron microscope was used to measure the carbon peak for these different materials. The powder samples were pressed into indium foil which was then placed onto a

stub. The microcalorimeter detector has a resolution of around 5 eV and 16 individual pixels each collecting a full spectrum. The individual spectra from each pixel were summed to obtain increased counting statistics for more accurate peak position measurements.

In examining the collected spectra for the materials mentioned, it was noted that the peaks are all downshifted from the expected 282 eV position. Secondly, each of the peaks has a distinct position and differences in shape indicating differences in the sp^2–sp^3 ratio for each material. A Gaussian fit to the peaks provides the peak positions. Using the amorphous carbon as the carbon reference point, the nanodiamond shows the largest shift toward higher energy relative to amorphous carbon. The graphite shows a small negative shift toward lower energy relative to amorphous carbon. The soot sample appears to be the most similar to the amorphous carbon, but does exhibit a small positive shift indicating potential nanodiamond character.

Preliminary theoretical simulations of the XES of these materials using the transition potential approximation in density functional theory indicate similar trends in both the shape and position of the peaks, and support the experimental measurements. We used simple molecular models for the systems of interest that are representative of the different local environments found around the excited centers. The theoretical results predict a clear relation between the shift relative to the graphite peak and the local out-of-plane distortion around the absorbing center, a quantity that is closely related to its sp^2–sp^3 character.

X-ray photoelectron spectroscopy provides the sp^2–sp^3 hybridizations through bombardment of the sample surface with X-rays that cause the subsequent release of electrons with the characteristic bonding energy of carbon: sp^2 at 284 eV and sp^3 at 285 eV. Graphite samples show purely sp^2 character, and nanodiamond shows a mixture of sp^2–sp^3 (26–39%). The soot sample is a majority 67% sp^2 with 16% sp^3 character. Raman spectroscopy provides further information as to the sp^2 allotropes and surface functionalization.

The microcalorimeter detector offers new X-ray measurement capabilities not found with conventional synchrotrons in that full spectra are measured compared with limited XANES scan ranges from synchrotron measurements. In addition, these measurements can be done within your laboratory.

References

(1) K. McIntosh, G. Havrilla, M. Croce, R. Huber, D. Podlesak, M. Rabin, F. Vila, M. Carpenter, and R. Cantor, "Study of Carbon Bonding with XES Using a TES Microcalorimeter Detector," to be presented at the 2017 Denver X-Ray Conference, Big Sky, Montana.

Kathryn McIntosh, George J. Havrilla, Mark Croce, Rachel Huber, David Podlesak, and Michael Rabin are with Los Alamos National Laboratory in Los Alamos, New Mexico. **Fernando Vila** is with the University of Washington, Seattle, Washington. **Matthew Carpenter and Robin Cantor** are with Star Cryoelectronics in Santa Fe, New Mexico.

Making X-ray Fluorescence Movies in the Laboratory Using CCD and CMOS Cameras

Kenji Sakurai and Wenyang Zhao

For many years, viewing elements as they move in chemical systems has been a dream for scientists. Because chemical reactions are coupled with the transportation and redistribution of elements, such a capability would be an excellent tool for elucidating many unknown phenomena in pure sciences as well as in medical and industrial applications. X-ray fluorescence (XRF) is a powerful nondestructive technique for determination of chemical composition. So far, however, capturing moving images with XRF, particularly in the laboratory, has been extremely challenging. Although we have reported the creation of some XRF movies using highly brilliant synchrotron sources (1,2), it is extremely important to enable similar experiments in ordinary laboratories, schools, industries, and hospitals. This year, at the Denver X-ray Conference, we will report our latest progress toward this goal (3,4).

Roughly speaking, in XRF, one can choose either a wavelength-dispersive X-ray spectrometer, which uses an analyzing crystal, or an energy-dispersive spectrometer equipped with a semiconductor detector such as a silicon drift detector. In XRF still-imaging, one typically uses an energy-dispersive spectrometer to obtain XRF spectra ef-

ficiently, while scanning the sample position with a small X-ray beam (created by using a focusing device such as mono- or polycapillary optics). The measurement time to obtain each individual image is quite long, and large pixel numbers are essential to provide enough information. In this situation, movie XRF imaging looks difficult. How can one collect many such XRF images as a function of time?

The key is to change the XRF imaging strategy. We propose a new approach, which we call projection-type XRF imaging, in contrast to scanning-type imaging. In this approach, instead of making xy scans with a micro X-ray beam, we use a rather large beam to illuminate the whole sample area. All XRF data are collected by an energy-dispersive two-dimensional (2D) detector. To project an XRF image onto the 2D detector plane, we have two options: parallel optics based on a collimator plate, or a simple pinhole camera. One of the remaining problems was how to make a 2D X-ray detector that has a large number of tiny pixels with sufficient energy resolution in the X-ray wavelength region.

There has been great progress in X-ray detectors. In the present research, we are using cooled charge-coupled-device (CCD) and complementary-metal-oxide-semiconductor (CMOS) cameras, which are designed for visible light applications. It is possible that other advanced 2D X-ray detectors could be used for XRF imaging, but we believe that the use of commercially available cooled CCD and CMOS cameras would be extremely convenient for many users, because they are not very expensive and are easy to obtain. One needs to remove the optical lenses as well as any covers, and affix an X-ray window there instead. The inside of the camera should be evacuated or at least replaced by dried gas because of the necessity of cooling.

Then the most likely next question is how to obtain X-ray energy information, which is absolutely necessary for XRF. In XRF instruments, as in other semiconductor detectors, X-ray photons create a large number of charges in a CCD or CMOS camera. Because the amount of charge corresponds to the energy of the X-rays, one can obtain information on impinged X-ray energy. This means that the intensity corresponds to the X-ray energy, if the image is read sufficiently quickly to avoid counting overlapped events. Such quick reading is often called single-photon counting. However, there are still some technical challenges. X-ray photons might not arrive at the center of the single pixel; for example, they may hit the corner of the pixel, in which case the created charges are eventually split into several pixels. Such events become more apparent when the pixel is small, particularly in the case of CCD and CMOS cameras made for visible light cameras. To deal with this problem of charge-sharing events, we are proposing a clever and fast filtering scheme.

At the 2017 Denver X-ray Conference, we will present our latest scientific XRF movies. For this work, we used a 1.5-kW

X-ray tube. The typical energy resolution of our system is around 150 eV@MnKα (depending on the cooling temperature). The spatial resolution is adjustable; we typically set it at 20–50 µm, depending on the XRF intensity of the sample. The time resolution for the movie is still not fast like a synchrotron experiment; it is on the order of a minute.

In our presentation, we will provide successful examples that visualize the real-time diffusion of elements such as calcium and iron in some chemical systems, from the beginning of the reaction to the end. One can understand how diffusion proceeds and how it depends on the element and matrix in real time. We hope this work will help to clarify the mechanism of chemical functions and reactions on a specific time scale. This novel XRF movie technique has the potential to open a new era of chemical science.

References

(1) K.Sakurai and H. Eba, *Anal. Chem.* **75,** 355–359 (2003). http://dx.doi.org/10.1021/ac025793h.

(2) K.Sakurai and M.Mizusawa, AIP Conference Proceedings 705 (Synchrotron Radiation Instrumentation 2003, San Francisco), pp. 889–892 (2004). http://doi.org/10.1063/1.1757938.

(3) W. Zhao and K. Sakurai, *Sci. Rep.* **7,** 45472 (2017). http://dx.doi.org/10.1038/srep45472.

(4) W. Zhao and K. Sakurai, *Rev. Sci. Instrum.* **88,** 063703 (2017). http://dx.doi.org/10.1063/1.4985149.

Kenji Sakurai, PhD, is the managing researcher at the Research Center for Advanced Measurement and Characterization at the National Institute for Materials Science in Ibaraki, Japan. **Wenyang Zhao** is a graduate student at the University of Tsukuba in Tsukuba, Japan.

High-Resolution X-ray Asymmetrical Reciprocal Space Mapping: A Technique for Structural Characterization of Semiconductor Superlattices

Andrian Kuchuk

Semiconductor superlattices (SLs), due to their unique electronic and transport properties, are nowadays commonly used for innovative optoelectronic devices and for high-frequency power electronics. Basically, SLs consist of a periodic arrangement of two semiconductor materials with different energy band gaps, with the SL period (T_{SL}) much larger than the semiconductor lattice constants. Because of the quantum size effects, the miniband structure of the SL depends not only on the semiconductors band gap, but also on the geometrical design of the SL. The properties of such quantum structures can be tuned in a wide range by changing the SL period, thicknesses, and strain state of quantum well (QW)–barrier layers. High-resolution X-ray diffraction (HR-XRD) is the main tool used to determine the superstructure parameters mentioned above. Com-

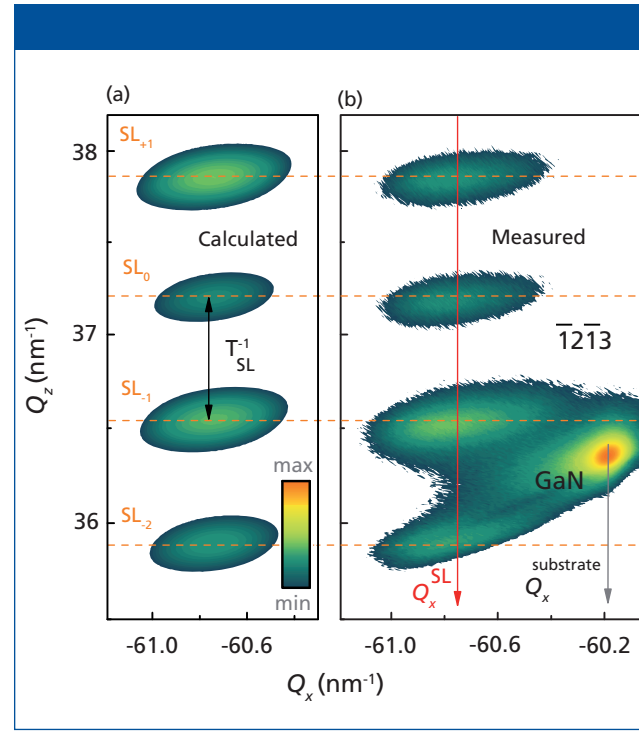

Figure 1: (a) Calculated and (b) measured $\bar{1}2\bar{1}3$ RSMs for 20 periods GaN–AlN SLs with the following superstructure parameters: T_{SL} = 9.46 nm; t_{GaN}/t_{AlN} = 4.38/5.08 nm; ε_x (GaN–AlN)= -3.05 × 10^{-3}/1.58 × 10^{-3}; N_{TD} = 3.32 × 10^8 cm^{-2}. The intensity is plotted in logarithmic scale.

monly (1–4), the reciprocal space map (RSM) of an asymmetrical reflection and the simulation of the measured ω/2θ X-ray diffraction profile (XDP) of a symmetrical reflection are used to evaluate the strain state and thicknesses of QW–barrier layers, respectively.

A novel approach has been proposed for structural characterization of semiconductor SLs using X-ray reciprocal space mapping of an asymmetrical reflection (5). The X-ray diffraction pattern of a periodic structure is characterized by a series of satellite peaks lying parallel to the modulation direction. In the reciprocal space, the distance between the satellite peaks corresponds to the reciprocal modulation period which is inversely proportional to T_{SL}. The positions of SL peaks depend both on the strain state and on the thickness ratio of QW–barrier layers. The new method relies on the determination of the satellite peak positions in reciprocal space and directly provides the superstructure parameters of the coherently grown SL. The considered method can be applied to any (strained or relaxed) SLs heteroepitaxially grown on the substrate.

Using the example of a GaN–AlN SL (5), it is demonstrated that the superstructure parameters obtained from the proposed method agree very well with the parameters revealed by the currently preferred approach that is based on the measurements and simulation of ω/2θ XDP of symmetrical reflections. Furthermore, by performing a simulation of the reciprocal lattice point broadening for an asymmetrical reflection (Figure 1), we additionally determined the density of threading dislocations (TDs) in GaN–AlN SL. The comparison of the density of TDs in the substrate and SL allows for analyzing the relaxation mechanism and developing a technique to improve the structural quality of the SL.

A simple method based on laboratory X-ray diffraction for nondestructive diagnostic purposes would be useful for design and precise growth of semiconductor superlattice-based devices. This new approach is not limited solely for III-nitrides; it can also be applied to a variety of materials. This method would be useful to the broad community of crystal growth, design, and epitaxy as a reliable growth calibration technique that does not waste valuable growth time or resources.

References

(1) F. Schubert et al., *J. Appl. Phys.* **115,** 83511 (2014).

(2) A.V Kuchuk et al., *Nanotechnology* **25,** 245602 (2014).

(3) M. Beeler et al., *Appl. Phys. Lett.* **105,** 131106 (2014).

(4) M. Tchernycheva et al., *Phys. Rev. B* **73,** 125347 (2006).

(5) H.V. Stanchu et al., *CrystEngComm* **19,** 2977 (2017).

Andrian Kuchuk, PhD, is the manager of the X-ray diffraction and Nanofabrication Laboratory at the Institute for Nanoscience and Engineering, at the University of Arkansas in Fayetteville, Arkansas. ■

Determination of Elemental Impurities in Antacids by ICP-MS According to the Validation Protocols Defined in *USP* Chapters <232> and <233> and *ICH* Q3D Step 4 Guidelines

This study focuses on the determination of a suite of Class 1 and 2A elemental impurities (Pb, As, Cd, Hg, Co, Ni, and V) in various over-the-counter antacid tablets by inductively coupled plasma–mass spectrometry (ICP-MS), as defined in the *United States Pharmacopeia* (*USP*) *Chapter* <232> and the *International Conference on Harmonization of Technical Requirements for Registration of Pharmaceuticals for Human Use* (*ICH*) *Step 4 Guidelines*. The analysis is performed according to the recommended sample preparation procedure and validation protocols laid out in *USP Chapter* <233>, by optimizing both the microwave digestion procedure and the analytical methodology for these types of sample matrices that contain extremely high levels of calcium, magnesium, and other mineral components.

Aaron Hineman

The *United States Pharmacopeia* (*USP*) (1) and *International Conference on Harmonization* (*ICH*) (2) have aligned the list and levels of 24 elemental impurities in pharmaceutical materials, which will be implemented on January 1, 2018. The elements of toxicological concern have been categorized into three groups based on their permitted daily exposure (PDE) levels, which are defined in *USP Chapter* <232> (3). To show compliance, manufacturers will need to measure the elemental contaminants by following the analytical methodology described in *USP Chapter* <233> (4). To supplement these new chapters, the United States Food and Drug Administration (FDA) also issued draft guidance recommendations for the pharmaceutical industry on elemental impurities in drug products that represent its current thinking on the topic from a regulatory perspective (5).

Elemental Impurities Analytical Methodology

USP General Chapter <233> recommends the use of either inductively coupled plasma–mass spectrometry (ICP-MS), inductively coupled plasma–optical emission spectroscopy (ICP-OES), or any other suitable technique that meets the necessary validation protocols, for the determination of elemental impurities in finished drug products. The analytical capabilities of ICP-MS make it the most suitable technique for performing determinations of the

Table I: A list of Class 1 and 2A impurities and their PDE limits defined *USP Chapter* <232> and *ICH Q3D Step Guidelines*

Element	Class	Oral Daily Dose PDE (µg/day)
Cd	1	5
Pb	1	5
As	1	15
Hg	1	30
Co	2A	50
V	2A	100
Ni	2A	200

Table II: Antacids chosen for this investigation

Antacid Type	Quantity	Description
Calcium based	2	Over-the-counter antacid tablet, containing only calcium
Magnesium based	1	Over-the-counter antacid tablet, containing only magnesium
Calcium and magnesium based	2	Over-the-counter antacid tablet, containing both calcium and magnesium
Others	3	Over-the-counter antacid tablets, containing other combinations of calcium, magnesium, sodium, or aluminum

Table III: Microwave digestion program for dissolution of antacid tablets

Step	Temperature (°C)	Pressure Max (bar)	Ramp (min)	Hold (min)	Power (%)
1	190	20	10	0	90
2	170	20	0	15	90
Cooling	50	20	1	15	0

Class 1 elements at these low levels on a routine basis—especially for drug products with a large daily dosage (>10 g/day). Among this category of medications and supplements, antacids present a unique set of analytical challenges for ICP-MS because of their extremely high calcium or magnesium content. High levels of total dissolved solids (TDS) can cause ionization suppression in the plasma as well as instrumental drift and increased maintenance because of deposition within the instrument. However, as shown in this work, these challenges can be overcome with optimized sample preparation and instrumental analytical conditions. A list of Class 1 and 2A impurities and their PDEs defined in *USP Chapter* <232> and *ICH Q3D Step Guidelines* appears in Table I.

Experimental

Sample Preparation

The eight antacids chosen for the evaluation represent a typical cross section of antacids available over the counter and are shown in Table II.

Microwave Digestion Procedure

USP Chapter <233> also makes suggestions on a closed-vessel or microwave digestion procedure to get solid samples into solution. A typical digestion for antacid samples uses nitric and hydrochloric acids, but because silica (SiO_2) is present in some of the samples, a source of fluoride is required to dissolve the silica—typically hydrofluoric acid or tetraethyl fluoroboric acid.

In this work, all samples were digested using a microwave digestion system (Titan MPS System, PerkinElmer Inc.) with standard 75-mL TFM (modified polytetrafluoroethylene) ves-

Compound Name: Antacids
Doses Per Day: 1
Weight Per Dose: 30 g
Amount Digested: 0.3 g
Final volume: 50 mL
Dilution: 1

Element	Oral Daily Dose PDE (µg/day)	J value (µg/L in solution)	Standard 1 (1.5 J [µg/L])	Standard 2 (0.5 J [µg/L])
Cd	5	1.0	1.5	0.5
Pb	5	1.0	1.5	0.5
Inorganic arsenic	15	3.0	4.5	1.5
Inorganic mercury	30	6	9	3
Co	50	10	15	5
V	100	20	30	10
Ni	200	40	60	20

Figure 1: Elements and standard concentrations calculated using PerkinElmer's J Value Calculator software.

Table IV: The ICP-MS instrument conditions used

Parameter	Value
RF power	1600 W
Plasma flow	15 L/min
Auxillary flow	1.2 L/min
Nebulizer gas flow	0.9 L/min
Helium gas flow	3.5 mL/min
AMS dilution	3x

sels. Approximately 3–5 g of material were crushed and homogenized. Then 0.30 ± 0.01 g of each sample was added to a digestion cup and placed in a digestion vessel, followed by 5 mL of nitric acid (70%), 1 mL of hydrochloric acid (35%), 1 mL of hydrogen peroxide (30%), and 0.5 mL of hydrofluoric acid (49%) when needed. The vessels were allowed to sit uncapped for 10 min to allow for any prereactions to occur safely before being capped and digested following the program in Table III. To evaluate the effect of the sample preparation on analyte recovery, spikes were added to the microwave vessel before the addition of acid.

When the digestion was complete, all samples were diluted with deionized water to a final volume of 50 mL, resulting in a total dilution factor of 167× with a reagent matrix of 10% HNO_3, 2% HCl, and 1% HF. Calibration standards were prepared in this same matrix. To stabilize mercury, 200 ppb gold (Au) was added to each sample, standard, and blank.

Instrumentation

For this validation, all analyses were performed on a NexION 2000 P ICP-MS system (PerkinElmer Inc.) (6) with a SMARTintro high-throughput and high-matrix sample introduction module using standard operating conditions. This configuration offers enhanced speed of analysis through the use of an in-line flow-switching valve and provides high matrix tolerance through the use of the all matrix system (AMS), which uses aerosol dilution for enhanced matrix tolerance. Although only vanadium (V), cobalt (Co), nickel (Ni), and arsenic (As) are affected by spectral interferences originating from the sample matrix and sample preparation procedure, the ICP-MS system was operated in collision mode for all analytes and samples, providing a simple method for the analysis. The instrument conditions are shown in Table IV, and the elements and masses appear in Table V.

Table V: Analytical masses and cell conditions used

Element	Mass (*m/z*)	Universal Cell Mode	Internal Standard
Na	23	Collision–helium	^{71}Ga
Mg	24	Collision–helium	^{71}Ga
Al	27	Collision–helium	^{71}Ga
Ca	43	Collision–helium	^{71}Ga
V	51	Collision–helium	^{71}Ga
Co	59	Collision–helium	^{71}Ga
Ni	60	Collision–helium	^{71}Ga
As	75	Collision–helium	^{72}Ge
Cd	111	Collision–helium	^{115}In
Hg	202	Collision–helium	^{159}Tb
Pb	206 + 207 + 208	Collision–helium	^{159}Tb

Table VI: Accuracy test: Predigestion spike recoveries in this antacid were all within the 70–150% acceptance criteria at all three spike levels

Element/ Mass	Mean Unspiked Sample		Mean Recovery (%)			Pass–Fail
	µg/g	J-value	50%	100%	150%	
V 51	0.218	<0.3J	96%	94%	97%	Pass
Co 59	0.039	<0.3J	91%	89%	88%	Pass
Ni 60	0.729	<0.3J	84%	82%	86%	Pass
As 75	0.102	<0.3J	97%	97%	109%	Pass
Cd 111	0.123	<0.3J	80%	81%	127%	Pass
Hg 202	0.005	<0.3J	91%	90%	86%	Pass
Pb 208	0.083	<0.3J	86%	84%	111%	Pass

Calibration

USP General Chapter <233> outlines the requirement to calibrate using a matrix-matched blank and calibration standards using concentration values of 0.5J and 1.5J. The *J-value* is defined as the permitted daily exposure limit for the element of interest, appropriately diluted to the working range of the instrument, after the sample preparation process is completed. In the case of antacids, large daily dosages are typical. For the eight samples in this study, the largest maximum dosage was 30 g of the antacid per day. Therefore, to test all samples using one set of calibration standards, a 30-g/day dosage was used in calculating the calibration range (0.5J and 1.5J). The elements and standard concentrations were calculated using PerkinElmer's J Value Calculator software, as shown in Figure 1.

USP General Chapter <233> also contains the following requirements for method validation:

- Accuracy: The matrix and materials under investigation must be spiked with target elements at concentrations that are 50%, 100%, and 150% of the maximum PDE. Mean spike recoveries for each target element must be within 70–150% of the actual concentrations.
- Repeatability: Six independent samples of the material under investigation must be spiked at 100% of the target limits defined and analyzed. The mea-

Table VII: Repeatability test: %RSDs for all target elements were well under the 20% acceptance limit

Element/ Mass	Sample 1 (µg/g)	Sample 2 (µg/g)	Sample 3 (µg/L)	Sample 4 (µg/g)	Sample 5 (µg/g)	Sample 6 (µg/g)	Mean (µg/g)	% RSD	Pass–Fail
V 51	3367	3424	3374	3370	3250	3342	3354	1.7 %	Pass
Co 59	1524	1522	1536	1514	1497	1494	1515	1.1 %	Pass
Ni 60	6285	6213	6231	6157	6081	6163	6188	1.1 %	Pass
As 75	591	584	580	582	577	595	585	1.2 %	Pass
Cd 111	265	257	257	250	260	264	259	2.0 %	Pass
Hg 202	900	915	902	893	890	920	903	1.3 %	Pass
Pb 208	225	225	222	218	221	228	223	1.6 %	Pass

sured percent relative standard deviation (%RSD) must not be more than 20% for each target element.

- Ruggedness: The repeatability measurement testing procedure should be carried out by analyzing the six repeatability test solutions either on different days, either with a different instrument or by a different analyst. The %RSD of the 12 replicates must be less than 25% for each target element.
- System suitability: Standard 1 (1.5J) must be measured before and at the end of analyzing a batch of samples. The difference between the two results must be less than 20% for each target element.

Results

All quantitative sample data were less than the 0.5J standard and, as a result, were less than the target limits for the elemental impurities. Therefore, for the purposes of this study, we chose to report the method validation results for the sample that produced the greatest matrix suppression of the internal standard signal. For this reason, one of the calcium- and magnesium-based over-the-counter tablet formulations was selected because it represented the most difficult analytical challenge out of all the samples examined.

Accuracy

The accuracy data of this antacid sample is exemplified in Table VI, which shows that the predigestion spike recovery test in the sample matrix passes at all three spike levels (50%, 100%, and 150% of the target limits) with the mean spike recoveries for each target element well within the 70–150% acceptance criteria.

Table VIII: Ruggedness test: The RSDs for the 12 measurements obtained on two different days were all well below the method requirement of 25%

Element/ Mass	Event 1- Spiked Sample at 100% of Target (µg/L)						Event 2- Spiked Sample at 100% of Target (µg/L)						Overall		
	1	2	3	4	5	6	7	8	9	10	11	12	Mean	%RSD	Pass–Fail
V 51	3367	3424	3374	3370	3250	3342	3247	3418	3327	3359	3276	3412	3347	1.8	Pass
Co 59	1524	1522	1536	1514	1497	1494	1580	1525	1558	1519	1485	1463	1518	2.1	Pass
Ni 60	6285	6213	6231	6157	6081	6163	6061	6202	6145	6137	6130	6293	6175	1.2	Pass
As 75	591	584	580	582	577	595	613	585	588	584	572	582	586	1.8	Pass
Cd 111	265	257	257	250	260	264	256	256	253	250	262	269	258	2.3	Pass
Hg 202	900	915	902	893	890	920	933	917	914	896	883	901	905	1.6	Pass
Pb 208	225	225	222	218	221	228	217	225	219	218	222	233	223	2.1	Pass

Table IX: System suitability test: The difference between the two results for each target element was less than 6%, which is well below the acceptance limit of 20%

Element/ Mass	Event 1				Event 2			
	Initial Standardization Solution 1 (µg/L)	Final Standardization Solution 1 (µg/L)	% Drift	Pass–Fail	Initial Standardization Solution 1 (µg/L)	Final Standardization Solution 1 (µg/L)	% Drift	Pass–Fail
V 51	29.8	29.6	-0.6%	Pass	30.4	30.2	-0.5%	Pass
Co 59	14.9	15.4	3.2%	Pass	15.1	14.6	-2.9%	Pass
Ni 60	60.0	62.2	3.5%	Pass	59.8	57.5	-3.9%	Pass
As 75	4.44	4.68	5.6%	Pass	4.53	4.59	1.2%	Pass
Cd 111	1.47	1.48	0.2%	Pass	1.53	1.57	2.6%	Pass
Hg 202	9.17	9.19	0.2%	Pass	8.87	8.86	0.0%	Pass
Pb 208	1.55	1.59	2.2%	Pass	1.48	1.51	2.2%	Pass

Repeatability

Six independently prepared samples of the Ca–Mg antacid were digested and then spiked at 100% of the target limit and analyzed. As shown in Table VII, the %RSDs for all target elements were within 2%, which is well under the 20% acceptance limit.

Ruggedness

The six samples used for the repeatability study shown in Table VII were analyzed on two different days. The RSDs for these 12 measurements are all <2.5% (as shown in Table VIII), well below the method requirement of 25%.

System Suitability

To accept the sample validation data, the instrument drift must be determined by measuring Standard 1 (1.5J) at the beginning and end of the analyses. The difference between the two results for each target element was less than 6%, which is below the acceptance limit of 20%, as demonstrated in Table IX.

Conclusion

This study has shown that the methodology easily handles these types of high-matrix antacid tablets. The Class 1 and 2A elemental impurity levels were well below the daily dosage PDE limits for *USP Chapter* <232> and *ICH Q3D Step 4 Guidelines* in the samples analyzed. In addition, to confirm the method validation, the most difficult antacid sample matrix was chosen and the method used for this work easily passed the acceptance criteria for the testing protocols described in *USP General Chapter* <233>.

References

(1) The United States Pharmacopeial Convention online: http://www.usp.org/usp-nf/key-issues/elemental-impurities.

(2) International Conference on Harmonization, *ICH Q3D Step 4 - Guideline for Elemental Impurities* (ICH, Geneva, Switzerland, 2014); http://www.ich.org/fileadmin/Public_Web_Site/ICH_Products/Guidelines/Quality/Q3D/Q3D_Step_4.pdf.

(3) General Chapter <232> "Elemental Impurities in Pharmaceutical Materials – Limits" in second supplement to *United States Pharmacopeia 39–National Formulary 34* (United States Pharmacopeial Convention, Rockville, Maryland, 2016); updates published in Pharmacopeial Forum 42(2).

(4) General Chapter <233> "Elemental Impurities in Pharmaceutical Materials – Procedures" in second supplement to *United States Pharmacopeia 38–National Formulary 33* (United States Pharmacopeial Convention, Rockville, Maryland, 2015).

(5) US Food and Drug Administration, *Guidance for Industry: Elemental Impurities in Drug Products* (FDA, Rockville, Maryland, 2016, https://www.fda.gov/downloads/Drugs/Guidances/UCM509432.pdf.

(6) "Thirty-Minute Guide to ICP-MS," PerkinElmer Technical Note, 2017, http://www.perkinelmer.com/lab-solutions/resources/docs/TCH-30-Minute-Guide-to-ICP-MS-006355G_01.pdf.

Aaron Hineman is with PerkinElmer Inc., in Shelton, Connecticut.
Direct correspondence to:
aaron.hineman@perkinelmer.com ■

Application of Wavelength-Dispersive X-Ray Fluorescence Spectrometry to Biological Samples

Wavelength-dispersive X-ray fluorescence (WD-XRF) spectrometry involves the classification and quantification of several kinds of biological samples. Multiple applications of WD-XRF spectrometry are anticipated in the mining industries, nuclear power industry, medical diagnostics, forensics, environmental, and particularly in agricultural studies. Here, we present a concise review of the quantitative measurements performed to classify and quantify the traces of essential and toxic minerals in wheat seed gall nematodes (*Anguina tritici*), *cyperus rotundus* rhizomes, gallstones, and kidney stones. Based on the studies reported, WD-XRF was found to be a robust analytical tool that is useful for agricultural studies and for the diagnosis of urological and gastroenterological disorders. This review is aimed at analyzing major and trace levels of heavy and toxic minerals in biological specimens related to agricultural crops (wheat grains and *cyperus rotundus*) and human diseases (gallstones and kidney stones) and shows some interesting prospects for using WD-XRF spectrometry.

Vivek K. Singh, Pradeep K. Rai, Ashok K. Pathak, Durgesh K. Tripathi, Subhash C. Singh, and Jagdish P. Singh

Trace and heavy metal detection in agricultural and biological samples currently is of crucial importance because of the pollution occurring in the environment, particularly in soil and water, which constantly affect human health. Agricultural crops, medicinal herbs, and natural resources used for human benefits are being contaminated by the presence of toxic elements such as lead, arsenic, mercury, chromium, and nickel. These elements then move from soils to plants and then to human beings. They can cause serious diseases such as cancer or stone formation in the human body (gallstones and kidney stones). Hence, a holistic approach is needed to analyze agricultural and biological samples to find the source of these toxic elements and take necessary steps for prevention.

Over the last few decades, the major aim of research in the field of agricultural and biomedical science has been to determine the concentrations of various toxic elements in many agricultural and biological specimens to find the cause of disease for its prevention. X-ray fluorescence (XRF) spectrometry is a versatile tool in many analytical problems. Major, minor, and trace elements can be qualitatively and quantitatively determined in various kinds of samples: metals, alloys, glasses, cements, minerals, rocks, ores, and polymers as well as environmental and biological materials (1). The application of wavelength-dispersive X-ray fluorescence (WD-XRF) spectrometry allows efficient determination of low-Z elements down to even beryllium (Be) without sample treatment with ensured high quality quantitative results. Because of the nondestructive character of X-ray measurement, XRF spectrometry is widely applied for the analysis of art, for example, museum and archeological objects such as manuscripts, paintings, icons, pottery, ancient glasses, ceramics, and coins.

XRF is based on the principle that all elements produce secondary "fluorescent" X-rays of characteristic energy when they

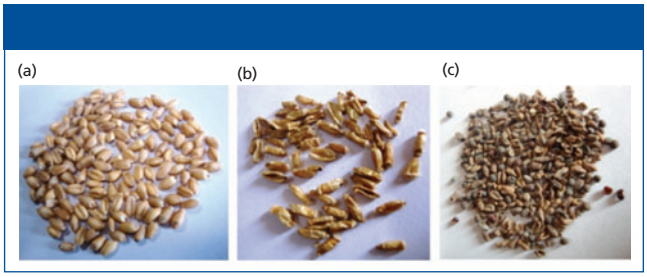

Figure 1: Photographs of (a) uninfected wheat grain, (b) wheat seed galls (low infection) with *Anguina tritici,* and (c) wheat seed galls (high infection) with *Anguina tritici*. Adapted with permission from reference 3.

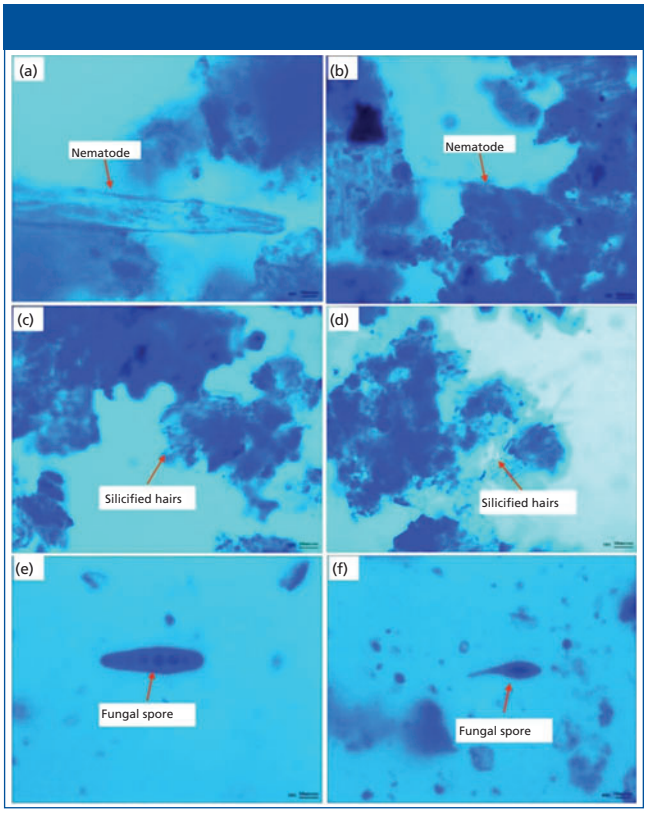

Figure 2: *Anguina tritici* (a, b), silicified hairs (c, d), helminthosporium (e), and alternaria (f). Adapted with permission from reference 3.

are exposed to X-rays of appropriate higher energy. The energy and intensity of the emitted X-rays can then be used to determine elemental composition. In principle, the higher the atomic weight of an element, the higher the energy needed to induce fluorescence and the fluorescence energy. It is also easier to detect fluorescence as the atomic weight of an element increases. Because XRF offers many unique capabilities, it has become the technique of choice for many applications requiring accurate elemental analysis for the purpose of meeting tight specifications at high concentration levels (2). High-performance WD-XRF spectrometry is now being used for the determination of traces in plant materials, biological samples, and geological samples. To fulfill today's requirements for quality data, modern instruments must provide high elemental sensitivities to achieve low detection limits and the best spectral resolution to minimize line overlays. In this article, we discuss the use of WD-XRF spectrometry to analyze trace and heavy metal contents in some agricultural and biological samples.

Materials and Method

The studied infected and uninfected wheat grain samples are shown in Figure 1. Figures 1a, 1b, and 1c are images of uninfected wheat grain, low infection wheat seed galls with *Anguina tritici (A. tritici)*, and high infection wheat seed galls with *A. tritici*. Microscopic observations revealed the infection in wheat samples with *A. tritici* and details can be found in the literature (3). Also, the galls have a similar shape to the uninfected grains but are dark brown in color. The studied *Cyperus rotundus* rhizome (belonging to the family *Cyperaceae*, which is widely distributed in many tropical and subtropical regions of the world) samples were collected and washed thoroughly to remove all the traces of soils and other possible contaminations. The biological applications and use of *Cyperus rotundus* can be found in the literature (4). The gallstones and kidney stone samples (5,6) studied using WD-XRF were collected from the Department of Nephrology at Opal Hospital in Varanasi, India.

To analyze the wheat samples, *Cyperus rotundus*, gallstones, and kidney stones, we used an S8 TIGER WD-XRF spectrometer (Bruker) for the determination of traces in these biological samples. The instrument was optimized to obtain better quantitative results, resolution, reproducibility, and reliability for each element with the best excitation and highest intensity over the whole elemental range. The quantitative measurements of the elemental constituents of kidney stones were performed using the same WD-XRF spectrometer. A 4-kW Rh anode X-ray tube (with a voltage of 60 kV max; and current 170 mA max) equipped with proportional flow counter and scintillation counter detectors was used as the energy source. Exposure time per sample was 20 min. The analyzer crystal LiF220 ensured that, in combination with the 0.23° collimator, the best separation was achieved for adjacent elements. The quantitative determination of major and trace elements was done using Quant-Express software (Bruker), which comprises a unique multipurpose preprepared calibration using certified standards. It automatically created the optimal measurement method to match each element and concentration range quickly, simply, and reliably.

Results and Discussion

Using WD-XRF to Analyze Uninfected and Infected Wheat Gall Nematodes

Microscopic observations (3) have been performed to identify nematodes in the infected wheat grains that clearly indicated the presence of dead nematodes and fungal spores inside the wheat galls. Figures 2a and 2b depict the nematodes identified as *A. tritici* while Figures 2c and 2d show the silicified hairs on the galls. Further, Figures 2e and 2f show the features identified as the fungal spores helminthosporium and alternaria, which originated from air during storage of the wheat grains and caused further grain damage.

The typical overlapped WD-XRF spectra of uninfected wheat grain and seed gall nematode (low and high infection) wheat

samples are shown in Figure 3 in different energy ranges. The relative intensities of the elements present in the uninfected, low infection, and high infection wheat samples are different, as can be seen in Figure 4, which indicates that their concentrations are different in different samples. The detected and quantified minerals in uninfected, low infection, and high infection wheat samples were potassium (K), sulfur (S), phosphorus (P), chlorine (Cl), calcium (Ca), magnesium (Mg), iron (Fe), silicon (Si), zinc (Zn), copper (Cu), sodium (Na), chromium (Cr), manganese (Mn), nickel (Ni), and aluminium (Al). The relative concentrations of these elements present in wheat samples are plotted in Figure 5. Among minerals, K, P, and S were predominant in uninfected grains as compared to Ca, Mg, Fe, Si, Cu, and Zn. The observed order of elemental concentration, particularly S, P, Ca, Mg, Fe, and Si, was found as follows: high infection wheat samples > low infected wheat samples > uninfected wheat samples. The concentration of K and Cl was highest in the low infection wheat sample. The concentration of Zn was higher for high infection wheat samples, a trend that may be correlated to the infection of grains caused by the nematodes. The elements Cr, Mn, and Ni were detected only in low infection and high infection wheat samples and they were completely absent in uninfected wheat samples which may be attributed to the activity of nematodes. Cu was only detected in uninfected and high infection wheat samples and was absent in low infection wheat samples. The mineral Na was only detected in low infection samples and Al was only detected in high infection wheat samples.

The toxic elements Al, Cr, and Ni were only detected in infected wheat samples and were not found in uninfected wheat samples. This result may be due to the presence of infected areas in grains because of the fungus and nematodes. The detected concentration of Al up to 600 ppm clearly indicated the toxic effect of Al in gall formation in wheat samples (7). Also, the presence of Cr and Ni at excessive levels in infected wheat samples were also the important reasons of gall formation in wheat grains. Thus, it was concluded that their presence was one of the factors leading to this disease and the formation of galls in wheat samples. The

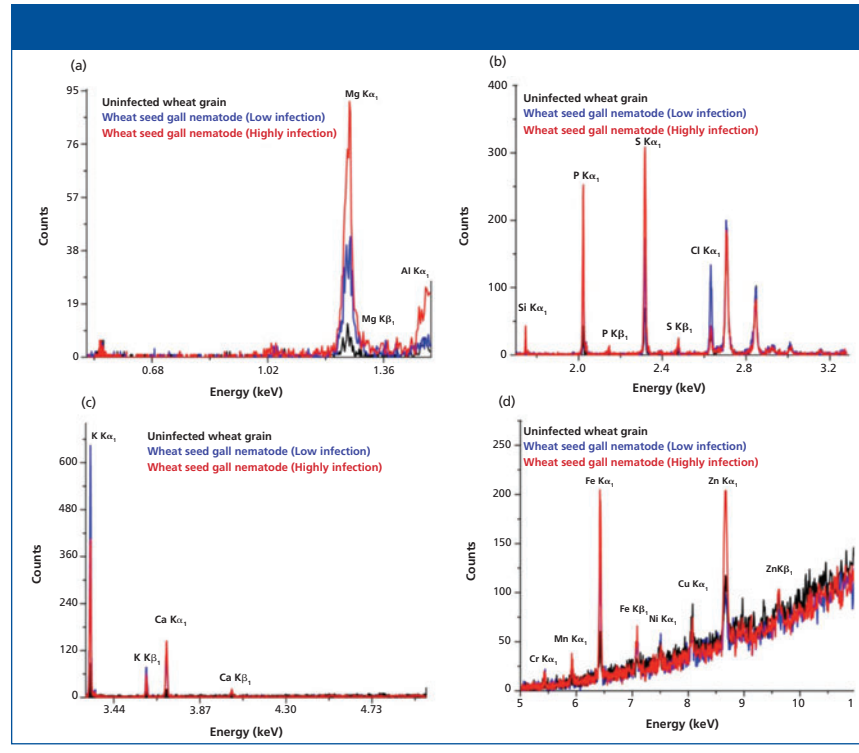

Figure 3: Typical WD-XRF spectra of uninfected and infected wheat grains in energy ranges (a) 0.5–1.5 KeV indicating the presence of Mg and Al; (b) 1.7–3.3 KeV indicating the presence of Si, P, S, and Cl; (c) 3.3–5 KeV indicating the presence of K and Ca; and (d) 5–11 KeV indicating the presence of Cr, Mn, Fe, Ni, Cu, and Zn. Adapted with permission from reference 3.

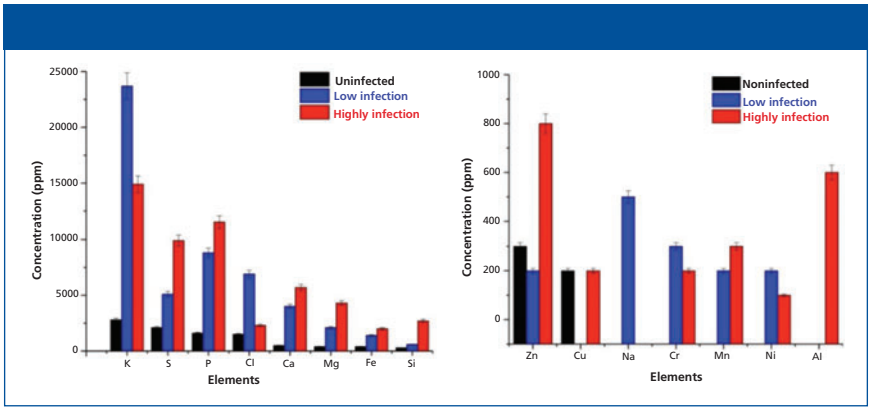

Figure 4: Bar diagrams showing the concentration of elements present in uninfected, low infection, and high infection wheat samples as measured using WD-XRF. Adapted with permission from reference 3.

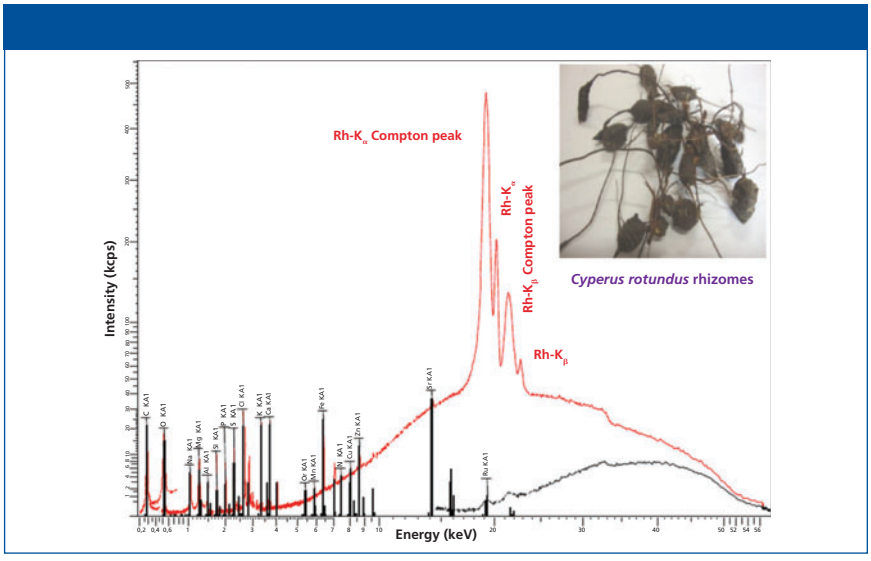

Figure 5: Typical WD-XRF spectrum of *Cyperus rotundus* (snapshot shown in inset) in different energy regions indicating the presence of macro- and micronutrient minerals. Details about spectral information can be found in reference 4.

maximum concentration of Zn high infection wheat samples was responsible for the change in color of infected wheat samples from light brown to black. Along with WD-XRF, the authors also applied Fourier transform infrared (FT-IR) spectroscopy to study the molecular compositions of the infected and uninfected wheat grain samples. Diffuse reflectance measurements of uninfected and infected wheat samples were also used to identify spectral differences among wheat samples.

The spectroscopic revolution has not only been regarded as the milestone for physical sciences, but also has opened the possibilities of new avenues in plant science and applied science. These findings underline the value of considerable supporting information using XRF spectrometry to avoid risks caused by microrganisms and are also helpful in avoiding damage to the environment, thus offering new investigation routes of agriculture- and disease-related issues.

Using WD-XRF to Analyze Minerals in *Cyperus Rotundus* Rhizomes

The high numbers of inorganic mineral elements present in nearly all plants ensure the successful growth and development of both vegetative and reproductive tissues. Currently, Fe, Zn, Mn, Cu, boron (B), Cl, molybdenum (Mo), and Ni have been recognized as micronutrients that are found at concentrations less than 0.01% of dry tissue weight (4). A few other minerals, such as cobalt (Co), sodium (Na), silicon (Si), selenium (Se), iodine (I), and vanadium (V), have also been shown to be essential and beneficial for certain plant species (4). Many other elements can be found in plants, but these are thought to enter plants nonselectively. Most of these nonessential elements confer no known benefit to the plant and many, such as cadmium (Cd) or Cr, are actually harmful to plant growth.

Cyperus rotundus Linn belongs to the *Cyperaceae* family and is widely distributed in many tropical and subtropical regions of the world. It is also known as purple nut sedge or nut grass and is a common weed found mostly in the fields, agricultural land, and moist waste land of all over India (4). The tubers of *Cyperus rotundus* have a wide range of medicinal and pharmacological applications. They are generally used as anthelmintic, aphrodisiac, diuretic, sedative, carminative, stimulant, tonic, and stomachic. They are also used as a remedy for renal colic and dysentery. Furthermore, the plant possesses different biological activities such as antioxidant, cytotoxic, antiallergic, antipyretic, anti-inflammatory, antiemetic, hypotensive, anticonvulsant, antimalarial, antimicrobial, antidiarrhoeal, antidiabetic, hepatoprotective, and insecticide (4).

The typical overlapped WD-XRF spectra of *Cyperus rotundus* samples are shown in Figure 5. The macro- and micronutrient minerals detected and quantified in *Cyperus rotundus* sample using WD-XRF were C, O, Na, Cl, Mg, Si, K, Ca, S, P, Al, Fe, Zn, Mn, Pd, Ru, Cr, Mo, Sr, Cu, and Ni. The concentrations of macronutrients Ca, Mg, K, P, and S were 0.36%, 0.46%, 0.38%, 0.20%, and 0.26%, respectively. The detected concentrations some micronutrients such as Al, Fe, Si, Na, and Cl were 0.06%, 0.05%, 0.42%, 0.8%, and 0.65%, respectively. Other micronutrients including some heavy minerals were detected at low levels ranging from 7 ppm to 44 ppm. The presence of elements found in *Cyperus rotundus* species were discussed in the literature (4). For the first-time, we used WD-XRF techniques to determine the macro- and micronutrient mineral contents of *Cyperus rotundus* rhizomes. Our results revealed that WD-XRF is a promising technique that is capable of analyzing plant samples with complex matrices used for medicinal purposes. Furthermore, the results obtained in the present paper show interesting prospects for WD-XRF to study plant samples. Other techniques, such as FT-IR and ultraviolet–visible (UV–vis) spectroscopy, have also been used for mo-

lecular analysis of *cyperus rotundus,* which revealed the capability of those techniques for the study of medicinal plants.

Using WD-XRF to Analyze Heterogeneous Gallstones

Stone formation (gallstone and kidney stones) inside human organs are common diseases and constitute a major health problem worldwide (8–10). These stones are the result of a buildup of chemical particles in the gallbladder and kidneys, respectively. The chemical composition of stones is complex and varied. Trace elements are essential components of biological structures and are necessary for a multitude of vital functions in the human body. The precise role of trace constituents in the pathogenesis of stones is still unclear and under debate, but researchers are increasingly focusing on the role of trace elements in their pathogenesis (8–10). To understand the formation of these stones and their growth, it is important to study their chemical and elemental compositions as well as the function of the different elements as affected by the stone type. Determining and studying the chemical composition of stones is often among urologists' main means of shedding light on the pathogenesis of stones. Analytical techniques such as atomic absorption spectroscopy (AAS), scanning electron microscopy coupled with energy-dispersive X-ray spectroscopy (SEM-EDX), XRF, proton-induced X-ray emission (PIXE), X-ray diffractometry (XRD), Raman spectroscopy and microscopy, FT-IR spectroscopy, and laser-ablation inductively coupled plasma–mass spectrometry (LA-ICP-MS) are currently being used to answer questions about the composition of stones worldwide (8,9). Routine analysis in the field of medical science is still based on X-ray, ion-beam, and spectroscopic techniques. Each technique has its own merits and demerits. Most of the recently developed optical techniques such as laser-induced breakdown spectroscopy (LIBS) are based on the detection of the radiation emitted by the elements present in the biological samples (8–10).

The WD-XRF spectra of these gallstone samples have been recorded and analyzed thoroughly (for more details see references 5 and 6). The major, trace, and heavy elements detected and quantified in gallstone (GS1, GS2, and GS3) were Ca, Na, K, P, Mg, Mn, Zn, Na, Cu, Fe, P, S, Si, Cl, Al, Br, Pd, and Ru. The relative concentrations of these elements are shown in the bar diagram in Figure 6. The observed concentrations of the elements Ca, Mg, Na, Cl, P, and S were higher in comparison to other elements. All other heavy elements were detected at trace amounts (parts-per-million range).

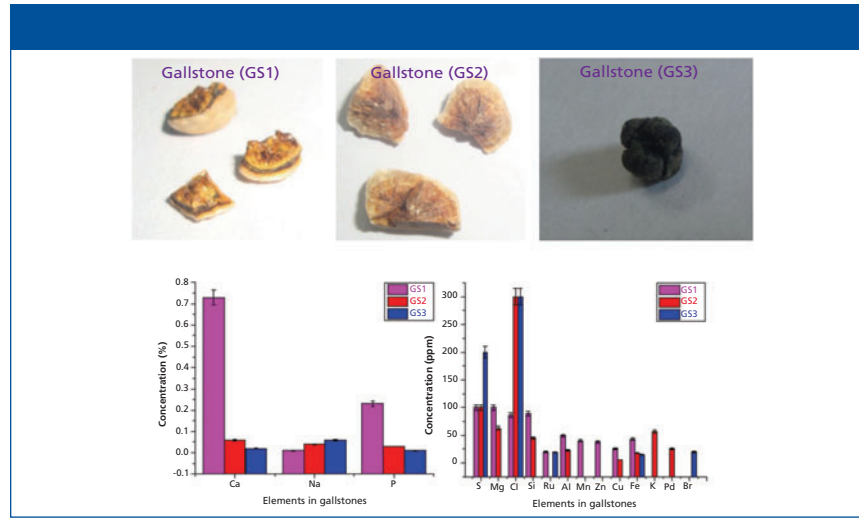

Figure 6: Gallstone samples and heavy and trace elements quantified using WD-XRF. Details and spectral information can be found in reference 5.

Figure 7: Photos of kidney stone samples. Adapted with permission from reference 11.

The presence of Na and Cl in higher amounts is because of the daily dietary consumption of NaCl (in the form of salt) by the patients, which deposited in ionic form in the stones during the initiation precipitation stage of the stone formation. Ca was found to be the predominant nonorganic constituent in all gallstones, which behaves as a nidus for the gallstone formation. The presence of Ca in higher amounts is mainly because of the type of food and drinks the patients take, including diary and milk products, eggs, tea, and hard water (5,6). An iron-deficient diet might alter the metabolism of the hepatic enzyme, which later increases gallbladder bile cholesterol and promotes cholesterol crystal formation. Furthermore, the central aggregates of calcium salts constitute hard foreign bodies that may lead to ulceration of the gall bladder mucosa, microscopic hemorrhage, and inflammation. This releasing process may be another source of Fe deposition in gallstones (5,6). Manganese (Mn) was also significant in the studied gallstones. Manganese forms a salt with bile acid, which gets accumulated during cholelithiasis. Gallstones also show the presence of some elements like Pd, Ru, and other trace elements using WD-XRF which may be due to the different geographical locations of patients with gallstones, the dietary differences of the patients, and environmental pollution issues.

In addition, we have also applied FT-IR spectroscopy to study the major presence

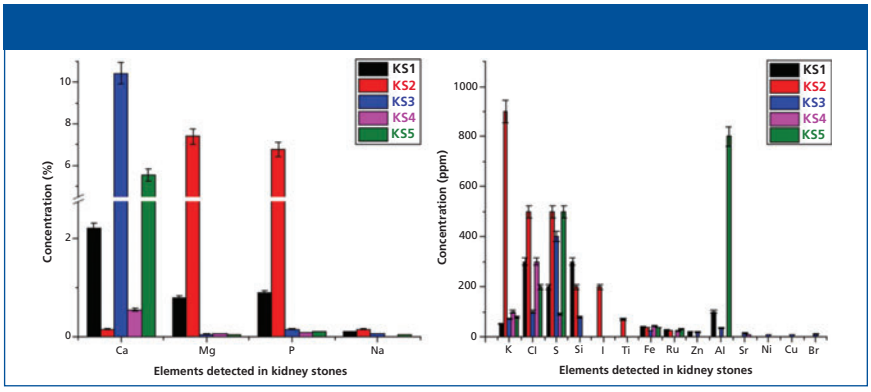

Figure 8: Relative concentrations of heavy and trace elements detected in kidney stones using WD-XRF spectrometry. Adapted with permission from reference 11.

of cholesterol and bilirubin, as well as the minor presence of calcium carbonate and calcium phosphate in gallstones. Our results revealed that FT-IR and WD-XRF are promising techniques that are capable of analyzing stone samples present inside the human body. The results obtained with this study show interesting prospects of WD-XRF to study cholelithiasis better.

Using WD-XRF to Analyze Traces in Kidney Stones

Kidney stones are a painful and prevalent disorder of the urinary system that is seen in patients throughout the world; its prevalence has drastically increased, particularly in industrialized countries. These stones are small, hard mineral deposits that build up on the inner surface of the kidney and grow rapidly because of the trace minerals in contact. Some minerals inhibit the growth of stones and others strengthen their growth rate depending upon the stone type. Hence, in this situation trace analysis of kidney stones becomes important to know its pathogenesis for prevention. Quantitative analysis of the stones removed from the body can not only be very valuable methods for the treatment of disease, but also to avoid conventional 24-h urine tests, which are generally complicated and imprecise. Despite several investigations about the elemental composition of kidney stones, there is insufficient information with regard to the distribution of trace elements in these stones, especially within the different stone types. Therefore, the present study (11) investigated various factors that play a regulatory role in the pathogenesis of two different kinds of kidney stones—oxalate stones and struvite stones—by using WD-XRF spectrometry.

The images of the kidney stone samples (KS1, KS2, KS3, KS4, and KS5) analyzed are shown in Figure 7. Clinical details of the patients can be seen in reference 11. FT-IR spectroscopy was used to classify the stone samples. The FT-IR spectral data indicated calcium oxalate monohydrate (COM) as the major constituent and calcium phosphate as the minor constituents of the kidney stones and hence stones (KS1, KS3, KS4, and KS5) could be classified as oxalate stones. Stone sample KS2 was identified as a struvite stone with the major presence of magnesium ammonium phosphate (MAPH), calcium phosphate, and the minor presence of COM.

The WD-XRF studies were performed on these two kinds of samples. The elements determined in stone samples (KS1–KS5) were Ca, Mg, P, Na, K, Cl, S, Si, I, Ti, Fe, Ru, Zn, Al, Sr, Ni, Cu, and Br. The relative concentrations of these elements are shown as a bar diagram in Figure 8. Detailed analysis of FT-IR and WD-XRF spectral studies can be seen in reference 11. I (200 ppm) and Ti (69 ppm) were detected only in sample KS2 in low concentration. Fe was detected in all stone samples and its concentration was found to be nearly comparable in all stone samples. No measurable differences of the concentration of Fe in stone samples was observed. Strontium (Sr) was detected only in KS3 and KS4, and heavy elements such as Ni, Cu, and Br were detected only in the oxalate stone sample (KS3).

The content of Mg and P was much higher in the struvite stone (KS2) than that of oxalate type stone samples (KS1, KS3–KS5). It is because of the stone matrix that magnesium ammonium phosphate ($MgNH_4.PO_4.6H_2O$) is called struvite. Ca was detected in all stone samples and was the major constituent of all kidney stones. However, the concentrations of Ca (0.55–10.42%) in oxalate type stone samples were higher than that of struvite stone (~ 0.15%). The concentration of Na, K, and Cl were also higher in the struvite stone samples than that of oxalate type stones. This higher concentration may be because of the higher presence of NaCl and KCl in struvite stone samples and indicates their role in struvite stones. For the first time, we have detected ruthenium (Ru) in all stone samples (except sample KS3) in low concentrations (ranging from 22 to 30 ppm). No measurable difference has been observed for Ru among the stones. Zn was only observed in oxalate type stone samples (KS1 and KS3) in low concentration (up to 20 ppm). The presence of Ru and Zn only in some stones is probably due to the dietary differences of the patients. We have also compared our results from the reported literature value of kidney stones using the XRF technique and good agreements were found (11).

We detected a wide range of elements —Ca, Mg, P, Na, K, Cl, S, Si, I, Ti, Fe, Ru, Zn, Al, Sr, Ni, Cu, and Br—in kidney stone samples. The concentration difference of the elements present in stones samples may be due to the different dietary habits of patients (vegetarian or nonvegetarian) as well as their differing environmental and geographical regions. Here, the stones samples collected were from patients from various regions or states of India with differing dietary habitats (11). Particularly, the studied stone samples were collected from the patients who were vegetarian and nonvegetarian. Also the patients have some habitats of nephrotoxins such as herbominerals, chewing tobacco products, and drinking alcohol.

Meats, meat products, and eggs are good sources of essential minerals not limited to Fe, Cu, Mg, Zn, and toxic and heavy metal elements particularly Pb, Co, Ni, and Br (12). Also, tobacco is indigenous to many areas such as India, the Middle East, Southeast Asia, and the Americas (13). The tobacco samples (spit tobacco, gutkaas, and paan masalas) were found enriched with the presence of mineral elements such as Na, K, Ca, Cl, Mg, P, Cu, Fe, and Zn and traces of toxic and heavy elements, particularly As, Cr, Co, Al, Ni, and Br (13). In our study, some heavy and toxic elements such

as Al, Cu, Ni, Br, and Sr were observed in the stone samples of patients with habits of chewing tobacco and meat products, which are potential sources of these heavy and toxic elements (13). The presence of toxic and heavy elements, particularly Ni, Br, and Cu, only in the KS3 stone sample may be due to the chewing habits because chewing samples were reported as enriched with these toxic elements (as mentioned earlier). Thus, it may be concluded that the presence of these elements in the samples may be due to chewing habits, alcoholic nature, and eating meat products. Along with these factors, the formation of stones in humans may also be influenced by the living style in a far more complex environment, drinking water, dietary differences, as well as genetic predisposition.

Conclusion

The spectroscopic revolution has not only been regarded as a milestone for physical sciences, but also has opened the possibilities of new avenues in plant science and applied sciences. We demonstrated several possibilities of using WD-XRF spectrometry for rapid analysis of some varieties of biologically important specimens such as wheat seed gall nematodes (*Anguina tritici*), *cyperus rotundus*, gallstones, and kidney stones. A significant advantage of this technique is that solid samples can be analyzed in their original unaltered condition, without undergoing pretreatment procedures. For the first time, we have successfully measured the concentrations of minerals such as K, S, P, Cl, Ca, Mg, Fe, Si, Zn, Cu, Na, and Mn in uninfected wheat grains along with some toxic elements such as Cr, Ni, and Al in infected wheat grains using WD-XRF. These findings underline the value of considerable supporting information through physical instruments to avoid risks caused by microorganisms and simultaneously help to avoid damage to the environment, thus offering new investigation routes of agriculture- and disease-related issues.

Using WD-XRF spectroscopy we have both analyzed and quantified a wide range of major and trace elements, including toxic elements in gallstones and kidney stones. We found the major differences between the elemental contents of calcium oxalate type stones and struvite stones. This study showed that the distribution and presence of elements in kidney stones are not only associated with geochemical factors but include environmental conditions and biology also. Occupations with higher insensible fluid losses, such as a hot environment, increase the risk of stone formation (14). The risk may also be higher when individuals have restricted access to water or bathroom facilities, leading to lower fluid intake and lower urine volume. In our study, the patients belong to different regions and different environments. In addition, dietary intake influences urine composition, thereby modifying the risk of nephrolithiasis. Heavy and toxic elements such as Al, Cu, Ni, Br, and Sr were found in the stones samples of the patients having habits of nephrotoxins (alcoholic, herbominerals, and chewing tobacco). In conclusion, the differences in the elemental concentrations in different stones may be correlated with the geographical, environmental, and dietary differences. More types of sample analysis is in progress by our research group.

WD-XRF is quite a suitable technique for in vitro quantitative analysis of both major and trace elements generally present in the samples of both gallstones and kidney stones. This technique has been applied uniquely to provide rapid qualitative and quantitative analysis of unknown environmental, biological, and medical samples including stone samples, in particular.

Acknowledgments

Vivek K. Singh is thankful to Mr. Tejbir Singh, in-charge WD-XRF Lab, SAIF, Punjab University, Chandigarh, India, facility for his valuable discussions and suggestions related to WD-XRF spectrometry and instrumentation. The author Dr. A.K. Pathak is grateful to University Grants Commission, New Delhi (F.No.8-4(57)/2015(MRP/NRCB) for financial assistance.

References

(1) M. West, A.T. Ellis, P.J. Potts, C. Streli, C. Vanhoof, and P. Wobrauschek, *J. Anal. At. Spectrom.* **31,** 1706–1755 (2016).

(2) J.A. Anzelmo, M. Bouchard, and M.È. Provencher, *Spectroscopy* **28,** 16–23 (2013).

(3) V.K. Singh, A. Devi, S. Pathania, V. Kumar, D.K. Tripathi, S. Sharma, D.K. Chauhan, V.K. Singh, and V. Zorba, *Biocatal. Agric. Biotechnol.* **9,** 58–66 (2017).

(4) V.K. Singh, A. Gupta, O. Gupta, V. Kumar, and M.A. Gondal, *Mat. Focu.* **6,** 7–14 (2016).

(5) B.B.S. Jaswal, J. Sharma, V. Kumar, Y. Khajuria, V.K. Singh, and P.K. Rai, *Adv. Sci. Lett.* **21,** 2613–2617 (2015).

(6) B.B.S. Jaswal, V. Kumar, J. Sharma, P.K. Rai, M.A. Gondal, Bilal Gondal, and V.K. Singh, *Lasers Med. Sci.* **31,** 573–579 (2016).

(7) N. Gupta, S.S. Gaurav, and A. Kumar, *Am. J. Plant Sci.* **4**(12), 21–37 (2013).

(8) V.K. Singh and P.K. Rai, *Biophy. Rev.* **6,** 291–310 (2014).

(9) A.K. Pathak, R. Kumar, V.K. Singh, R. Agrawal, S. Rai, and A.K. Rai, *Appl. Spectrosc. Rev.* **47,** 14–40 (2012).

(10) V.K. Singh, V. Singh, A.K. Rai, S.N. Thakur, J.P. Singh, and P.K. Rai, *Appl. Opt.* **47,** G38–G47 (2008).

(11) V.K. Singh, B.B.S. Jaswal, J. Sharma, and P.K. Rai, *X-Ray Spectrom.* **46,** 283–291 DOI: 10.1002/xrs.2775 (2017).

(12) M.Z.A. Chowdhury, Z.A. Siddique, S.M.A. Hossain, A.I. Kazi, M.A. Ahsan, S. Ahmed, and M.M. Zaman, *J. Bangladesh Chem. Soc.* **24,** 165–172 (2011).

(13) A.N. Garg, R.P. Choudhury, R. Acharya, and A.V.R. Readdy, *J. Radioanal. Nucl. Chem.* **294,** 197–202 (2012).

(14) L. Atan, C. Andreoni, V. Ortiz, E.K. Silva, R. Pitta, F. Atan, and M. Srougi, *Urol.* **65,** 858–861 (2005).

Vivek K. Singh is with the Department of Physics at Shri Mata Vaishno Devi University in Jammu and Kashmir, India. **Pradeep K. Rai** is with the Department of Urology and Nephrology at Opal Hospital in Varanasi, India. **Ashok K. Pathak** is with the Department of Physics at Ewing Christian College, University of Allahabad in Allahabad, India. **Durgesh K. Tripathi** is with the Centre for Medical Diagnostic and Research (CMDR), MNNIT Allahabad in Allahabad, India. **Subhash C. Singh** is with The Institute of Optics at the University of Rochester in Rochester, New York. **Jagdish P. Singh** is with the Institute for Clean Energy Technology at Mississippi State University in Starkville, Mississippi. Direct correspondence to: vivekksingh2005@gmail.com ■

PRODUCTS & RESOURCES

XRF kit

Amptek's XRF kit is designed to help users quickly begin doing elemental analysis via X-ray fluorescence. According to the company, the kit includes the company's X-123 complete spectrometer with a FAST SSD or SSD detector, a Mini-X USB Controlled X-ray tube, XRF-FP QA software, a sample enclosure, and test sample.
Amptek, Inc.,
Bedford, MA;
www.amptek.com

XRF measurement systems

The SMX X-ray fluorescence thickness and composition measurement systems from EDAX are designed to measure a variety of inorganic coatings at the laboratory bench or on the factory floor. According to the company, the systems are available in various configurations to measure photovoltaics, aluminum, and other metal treatments.
EDAX, Inc.,
Mahwah, NJ;
www.edax.com

Calibration standards

Calibration standards from Micromatter Technologies are designed for X-ray fluorescence analysis. According to the company, thin film standards are prepared by vacuum deposition, which results in a uniform deposit, ranging from 0.5 to 120 µg/cm^2; RoHS analysis standards contain elements such as Cr, As, Br, Cd, Hg, Pb, and Sn; and thick standards are 99.999% pure self-supporting foils with thicknesses ranging from 0.5 µm to several micrometers. **Micromatter Technologies, Inc.,** Surrey, BC, Canada; www.micromatter.com

Diffuse reflectance probe

The Ocean Optics diffuse reflectance probe is designed to measure 45° diffuse reflectance for UV–vis and NIR spectroscopy. According to the company, the probe removes localized variance in reflectance measurements and is suitable for applications such as color analysis, material identification, and quality monitoring of grains and other foods.
Ocean Optics,
Dunedin, FL;
www.oceanoptics.com

Autosampler

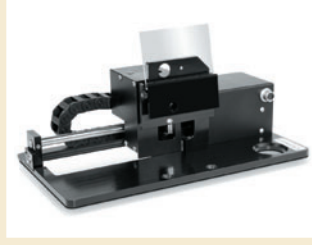

The YZ autosampler from PIKE Technologies is designed for sample transmission measurements where precise mapping is required. According to the company, the autosampler fits in the sample compartment of most FT-NIR and FT-IR spectrometers, and its Y and Z plane movement (no rotation) makes it a suitable accessory for spectroscopic measurements of samples having a spectral signature influenced by orientation, such as a polarized film.
PIKE Technologies, Madison, WI;
www.piketech.com

Benchtop XRD system

Rigaku's MiniFlex benchtop X-ray diffraction system is designed for phase identification and quantification, and the determination of percent (%) crystallinity, crystallite size and strain, lattice parameter refinement, Rietveld refinement, and molecular structure. According to the company, the system can be used in research in material science and chemistry, and in industry for research and quality control.
Rigaku Corporation,
Tokyo, Japan;
www.rigku.com

Multimodal Raman spectrometer

Thermo Fisher's iXR Raman spectrometer is designed with optical interfacing to simultaneously provide a chemical fingerprint and material structure data while gathering elemental or physical information from complementary instrumentation that provides correlation of data. According to the company, the spectrometer can capture spectroscopic changes over time, enabling measurement of dynamic processes or changing conditions, such as the crystallization of a polymer in a rheological study. **Thermo Fisher Scientific,** San Jose, CA;
www.thermoscientific.com/raman

Raman spectrometer

B&W Tek's iRaman Pro ST portable Raman spectrometer is designed to measure through a variety of materials. According to the company, the spectrometer can measure through clear or semitransparent containers, white and red plastics, pill coatings, yellow and manila colored paper, white packaging envelopes, and glass.
B&W Tek,
Newark, DE;
www.bwtek.com

Raman imaging software

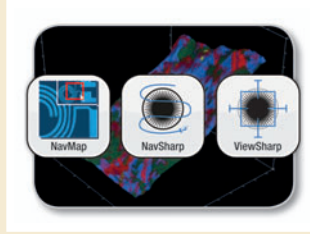

HORIBA's EasyNav software reportedly includes three applications: the NavMap video feature, which shows the global sample and the zoomed region of interest within the sample, simultaneously, in real-time; NavSharp, which provides sharp and real-time navigation on a sample image with any topography; and ViewSharp, which constructs an image in which all surfaces are in focus simultaneously and creates a 3D topography image.
HORIBA Scientific, Edison, NJ; horiba.com/easynav

Microwave digestion

Milestone's UltraWAVE microwave digestion system uses the company's single reaction chamber technology for metals digestions. According to the company, the system uses a single pressurized vessel for all samples, allowing for simultaneous digestion of up to 22 samples. The system reportedly can accommodate a maximum temperature of 300 °C and pressure of 199 bar.
Milestone, Inc., Shelton, CT; www.milestonesci.com/ultrawave

ICP-MS system

Shimadzu's ICPMS-2030 inductively coupled plasma–mass spectrometry system is designed for environmental testing, food and agriculture studies, and pharmaceutical work. According to the company, the system includes assistant functions that develop methods and perform post-run diagnostics.
Shimadzu Scientific Instruments, Columbia, MD; www.ssi.shimadzu.com

Infrared beamsplitters

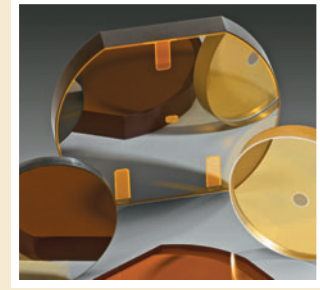

Photon Pro infrared beamsplitters from Spectral Systems are designed for use in the analysis of hazardous materials, environmental control, process control, and material recognition on the manufacturing floor. According to the company, the beamsplitters simultaneously transmit and reflect 50% of the incident beam between two optical elements.
Spectral Systems LLC, Hopewell Junction, NY; www.spectral-systems.com

Deep UV certified reference material

A certified reference material (CRM) from Starna Scientific is designed to qualify a UV spectrophotometer in the deep UV. According to the company, the CRM can provide reliable qualification data below 200 nm, and a new reference material (TS8) was developed with suitable spectral characteristics in the region of 190–230 nm.
Starna Cells, Inc., Atascadero, CA; www.starna.com

X-ray coating thickness gauges

Hitachi's FT150 X-ray coating thickness gauges are designed to measure plating thickness and composition at micro spots with diameters less than 100 µm. According to the company, the gauges have polycapillary optics composed of several thousand glass capillary tubes that work like a convex lens to focus X-rays.
Hitachi Technologies America, Inc. Dallas, TX; www.hitachi-hta.com

Raman spectrometers and systems

Wasatch Photonics Raman spectrometers and systems are designed with a high NA input and transmissive VPH gratings to reduce acquisition time. According to the company, fiber-coupled, free space, and integrated laser modes are available with excitation wavelengths ranging from 405 nm to 1064 nm and are configurable for range, resolution, and degree of detector cooling.
Wasatch Photonics, Durham, NC; www.wasatchphotonics.com

Hyphenated thermal analysis systems

PerkinElmer's hyphenated thermal analysis systems reportedly consist of two or more instruments coupled to increase the power of analyses and save time by acquiring more information from a single run. According to the company, its TGA 8000 thermogravimetric analyzer and STA simultaneous thermal analyzer, coupled with FT-IR, MS, or GC–MS instruments, provide analyses for materials characterization in polymers, pharmaceuticals, chemicals, petroleum, rubber, and food.
PerkinElmer, Waltham, MA; www.perkinelmer.com/hyphenation

Ad Index

FACSS Presents

THE GREAT **SCI**ENTIFIC E**X**CHANGE

SCIX2017

THE PREMIER MEETING FOR ANALYTICAL CHEMISTRY AND APPLIED SCIENCES

GRAND SIERRA RESORT • RENO, NEVADA

OCTOBER 8 - 13, 2017

SciX is presented by

Federation of Analytical Chemistry and Spectroscopy Societies (FACSS) and its 13 Member Organizations

Leading researchers will convene to present their cutting edge developments in analytical instrumentation and their wide-ranging applications.

Plus exciting new WORKSHOPS for Career Development

CONFERENCE TOPICS

Atomic Spectroscopy | Chemical Imaging | Chemometrics for Spectroscopy

Contemporary Issues in Analytical Science | Fluorescence Spectroscopy | Forensic Sciences

Infrared Spectroscopy | Laser Induced Breakdown Spectroscopy | Mass Spectrometry | Microscopy

Near Infrared Spectroscopy | Process Analytical Technology | Raman Spectroscopy

Spectroscopic Bioanalysis | Spectroscopic Pharmaceutical Analysis | Standoff Sensing

Surface Plasmon Resonance Spectroscopy | Terahertz Spectroscopy

KEYNOTE SPEAKER

Janie Dubois

University of Maryland, JIFSAN

Chair of the Laboratory Capacity Working Group at the World Bank's Global Food Safety Partnership

"The analytical and economic challenges of maintaining food safety in a global supply chain"

Join with Members of the Thirteen International Societies of the FACSS Family and see why SciX is the 'Right Size, Right Science, Right Conference.'

SciXConference.org

MEMBER ORGANIZATIONS:

American Chemical Society Division of Analytical Chemistry

AES Electrophoresis Society

American Society for Mass Spectrometry

ANACHEM

Austrian Society of Analytical Chemistry

Coblentz Society

Council for Near Infrared Spectroscopy

Infrared and Raman Discussion Group

International Society of Automation-Analysis Division

North American Society for Laser-Induced Breakdown Spectroscopy

Royal Society of Chemistry

Society for Applied Spectroscopy

The Spectroscopical Society of Japan

NATIONAL MEETING:

Society for Applied Spectroscopy (SAS)

and

North American Society for Laser-Induced Breakdown Spectroscopy (NASLIBS)

SPECIAL TOPICS FOR 2017:

- Modern Techniques in Microscopy
- Standoff Sensing
- Contemporary Challenges in Analytical Science

FACSS
2019 GALISTEO ST. BLDG. I-1
SANTA FE, NM 87505 (USA)
(505) 820-1648
SciX@SciXConference.org

ANY MATRIX
ANY INTERFERENCE
ANY PARTICLE SIZE

NexION 2000 ICP-MS: Triple quad power meets single quad versatility.

Trace metals in food, nanomaterials in water, impurities in everything from pills to electronic components: These are the sweet spot for the NexION® 2000 ICP-MS. Its sample introduction technology lets you run samples with up to 35% total dissolved solids. Plus, its interference removal capabilities give you the best detection limits for your application. And it delivers superior analysis times and single particle/cell detection capability – at least 10x faster than competitive systems. So the NexION 2000 ICP-MS is up to the most important challenge of all: ***Yours.***

For more information,
visit perkinelmer.com/NexION2000

NexION 2000 ICP Mass Spectrometer

PerkinElmer®
For the Better